Atmos. Meas. Tech. Discuss., 7, 10829–10881, 2014
www.atmos-meas-tech-discuss.net/7/10829/2014/
doi:10.5194/amtd-7-10829-2014

Atmospheric Measurement Techniques Discussions
Open Access

Atomic oxygen retrievals in the MLT region from SCIAMACHY nightglow limb measurements

O. Lednyts'kyy[1], C. von Savigny[1], K.-U. Eichmann[2], and M. G. Mlynczak[3]

[1]Institute of Physics, Ernst-Moritz-Arndt-University of Greifswald, Greifswald, Germany
[2]Institute of Environmental Physics, University of Bremen, Bremen, Germany
[3]NASA Langley Research Center, Hampton, Virginia, USA

Received: 10 September 2014 – Accepted: 10 October 2014 – Published: 30 October 2014

Correspondence to: O. Lednyts'kyy (olexandr.lednytskyy@uni-greifswald.de)

Published by Copernicus Publications on behalf of the European Geosciences Union.

Abstract

Vertical profiles of atomic oxygen concentration in the mesosphere and lower thermosphere (MLT) region were retrieved from sun-synchronous SCIAMACHY/Envisat limb observations of the oxygen 557.7 nm green line emission occurring in the terrestrial nightglow. A band pass filter with noise detection was applied to eliminate contributions from other emissions, the impact of noise and auroral activity. Assuming horizontal homogeneity of each atmospheric layer, and absence of absorption and scattering, vertical volume emission rate profiles were retrieved from integrated limb emission rate profiles. The radiative transfer problem was treated with a linear forward model and inverted using regularized total least squares minimization. Atomic oxygen concentration ([O]) profiles were retrieved at altitudes from 85 to 105 km with approximately 4 km vertical resolution for the period from August 2002 to April 2012 at a constant local time (LT) of approximately 22:00. The retrieval of [O] profiles was based on the generally accepted 2-step Barth transfer scheme including consideration of quenching processes and the use of different available sources of temperature and atmospheric density profiles. A sensitivity analysis was performed for the retrieved [O] profiles to estimate the maximum uncertainty, assuming independent contributions of uncertainty components. The retrieved [O] profiles were compared with reference [O] profiles measured by SABER/TIMED and modelled using NRLMSISE-00 and SD-WACCM4. A comparison of the retrieved [O] profiles with the reference [O] profiles enabled the selection of the most appropriate photochemical model accounting for quenching processes and the most appropriate source of temperature and density profiles for further application of our approach to the [O] profile retrieval. The obtained [O] profile time series show characteristic seasonal variations in agreement with atmospheric models and satellite observations based on analysis of OH Meinel band emissions. Furthermore, a pronounced 11 year solar cycle variation can be identified in the atomic oxygen concentration time series, which will be the subject of further studies.

AMTD
7, 10829–10881, 2014

1 Introduction

Atomic oxygen (O) is the most abundant chemically active trace gas in the Earth's mesosphere-lower thermosphere (MLT) region. It plays a critical role for O_3 and indirectly for OH^* formation as well as the energy balance in the MLT region. Being generated through photolysis of molecular oxygen by ultraviolet radiation during daytime, atomic oxygen is subsequently destroyed through three-body recombination and other chemical processes. Atomic oxygen fuels exothermic chemical reactions (Mlynczak and Solomon, 1993) and causes radiative cooling of the MLT region that occurs through collisions of O with molecules (CO_2, NO), later resulting in infrared emissions (Jursa, 1985). The green line emission of O(^{1}S–^{1}D) is visible at night due to the long photochemical lifetime (on the order of months at 100 km altitude) of ground state atomic oxygen O(^{3}P) which is excited to O(^{1}S) through the two step process known as the Barth transfer scheme.

Decades of ground-based observations of the O(^{1}S) airglow emission rate (first performed by the 4th Lord Rayleigh in 1928, Egerton, 1949) were followed by rocket measurements. Ground-based observations of integrated airglow emission rates are constrained by specific geophysical locations for a given day. A limited number of direct measurements of atomic oxygen concentration ([O]) profiles (McDade et al., 1986; Iwagami et al., 2003; Yoshimura et al., 2003; Melo et al., 1996; Gobbi et al., 1992; Kita et al., 1992) were performed to support the hypothesis that a Barth-type mechanism is involved in producing O(^{1}S) in the MLT region. Simultaneous direct measurements of atomic oxygen density and nightglow emission rate profiles were provided by the Energy Transfer in the Oxygen Nightglow (ETON) rocket campaign to develop the well known empirical airglow models (e.g., McDade et al., 1986).

Satellite limb measurements of the atomic oxygen 557.7 nm green line emission rates enable retrieving [O] profiles continuously and on a near-global basis. The Scanning Imaging Absorption spectroMeter for Atmospheric CHartographY (SCIAMACHY) examining the atmosphere in a dedicated limb mesosphere/thermosphere

AMTD
7, 10829–10881, 2014

mode enables vertically resolved measurements of the nightglow green line emission. On the basis of the obtained measurements the retrieval of [O] profiles is possible.

The basic purpose of our study is such a retrieval of [O] profiles in the MLT region within the time period from August 2002 to April 2012 at approximately 22:00 LT. The retrieval was performed according to the following scheme. The O(^{1}S) nighttime green line spectra measured by SCIAMACHY were averaged (see Sect. 2.1) and integrated to limb emission rate (LER) profiles in five degree latitude bins with daily and monthly resolution (see Sect. 3). Vertical volume emission rate (VER) profiles were retrieved from LER profiles applying linear inversion supported by regularized total least squares (RTLS) minimization (see Sect. 4). The well known cubic equation (McDade et al., 1986) and its extension (Gobbi et al., 1992; Semenov, 1997; Khomich et al., 2008) were used to retrieve [O] profiles (see Sect. 5) on the basis of temperature and density profiles provided by different available sources and VER profiles retrieved from SCIAMACHY nightglow observations. Temperature and density profiles were provided by the NRLMSISE-00 atmospheric model (Picone et al., 2002), the SD-WACCM4 climate model (Liu et al., 2007) and by measurements with the SABER instrument on the TIMED spacecraft (Russell et al., 1999).

Random and systematic errors were estimated for the obtained data sets at each step of the retrieval. The uncertainty components were assumed to contribute to the total error independently. Successive linear addition of the estimated uncertainty components (Kennedy et al., 2011) was performed at each step of the retrieval procedure to calculate the maximum error. A verification of the retrieved [O] profiles was performed through their comparison with reference [O] profiles provided by the NRLMSISE-00 and SD-WACCM4 models as well as SABER retrievals (see Sect. 6). The selection of the appropriate photochemical model (cubic or extended cubic equation) and the choice of the appropriate source of temperature and density profiles was made at the corresponding steps of the verification.

The optimized [O] retrieval (based on VER profiles provided by SCIAMACHY measurements, see Sect. 5) might also be applied to VER profiles provided by other satellite

AMTD
7, 10829–10881, 2014

instruments (e.g., WINDII, OSIRIS, ISUAL) if the measurement data were available. Hydroxyl and oxygen green line nightglow observations from the Wind Imaging Interferometer (WINDII) on board the Upper Atmosphere Research Satellite from 1991 to 2004 were already used to retrieve [O] profiles (Russell et al., 2005). Daytime and nighttime O_2 A-band airglow measurements with the Optical Spectrograph and Infrared Imaging System (OSIRIS) on board the Odin satellite from 2001 to date were also used to retrieve [O] profiles (Sheese et al., 2011). Gao et al. (2012) used green line airglow measurements with the Imager of Sprites and Upper Atmospheric Lightning (ISUAL) on board the FORMOSAT-2 satellite to retrieve [O] profiles. In a very recent study, SCIAMACHY O(^{1}S) green line observations were employed by Kaufmann et al. (2014) in combination with a slightly modified version of the McDade et al. (1986) photochemical model to retrieve atomic oxygen profiles. Differences between the Kaufmann et al. (2014) retrieval and the one presented in this study will be discussed below in Sect. 7.3.

2 Description of instruments and models used

2.1 SCIAMACHY on board the satellite Envisat

The Environmental Satellite (Envisat-1) designed by the European Space Agency (ESA) carries 10 instruments (total weight about eight tons). One of them, the Scanning Imaging Absorption spectroMeter for Atmospheric CHartographY (SCIAMACHY) (Burrows et al., 1995; Bovensmann et al., 1999), observed the radiation field in limb, nadir, and solar/lunar occultation geometry. On 1 March 2002 Envisat was launched into a sun-synchronous orbit with an inclination of 98.5° and a period of 100 min, thus performing about 14.4 orbits per day at a mean altitude of 799.8 km (Gottwald et al., 2006). The grating spectrometer SCIAMACHY provided measurements in eight spectral channels within a wavelength range from 220 to 2380 nm and 0.22–1.48 nm spectral resolution.

AMTD
7, 10829–10881, 2014

The limb-emission observations on the Earth's nightside additionally performed by SCIAMACHY at a fixed local solar time (around 22:00 LT) were used in the study presented here. This dedicated mesosphere/thermosphere mode, covering the 75–150 km tangent height (TH) range, is characterized by a nominal difference between two adjacent tangent heights of 3.3 km and 0.045° vertical field of view (Cardaci, 2010; Kaiser et al., 2004). The geometrical field of view is approximately 2.4–2.6 km in vertical direction at the tangent point depending on tangent height and satellite position (Kaiser et al., 2004). Note that the SCIAMACHY nighttime limb emission measurements are only performed continuously throughout the year at latitudes between 0 and 30° N.

The communication link to Envisat-1 and hence SCIAMACHY operations was interrupted in April 2012. The nighttime limb measurements from August 2002 to April 2012 were pre-processed by the German Aerospace Center (DLR) and data quality reports (SOST-DLR, 2013a, b, c) and data anomaly reports (SOST-DLR, 2012) were provided. The data used in our study were pre-processed from Level 1c SCIAMACHY format to the orbital measurements of the green line emission spectra. Level 1 data version 7.0x were used in this study and the data were calibrated using all calibration flags. The spectral resolution of the SCIAMACHY spectra in channel three used in this study is about 0.2 nm.

2.2 SABER on TIMED

The Sounding of the Atmosphere using Broadband Emission Radiometry (SABER) infrared radiometer on board the NASA TIMED satellite measures a number of middle atmospheric parameters and NASA provides data via the Internet (SABER, 2014). SABER measurements are made within the latitude range 54° S–87° N or 87° N–54° S with coverage alternating every 60 days. The vertical resolution of SABER measurements is approximately 2 km (Mertens et al., 2009). Nighttime hydroxyl emission rates measured with SABER are used to calculate atomic oxygen mixing ratios (Mlynczak et al., 2013). In our study SABER level 2A data (version 2.0) for the years 2002–2012 were interpolated to 1.0 km altitude grid resolution and averaged within the

AMTD
7, 10829–10881, 2014

time interval 21:00–23:00 LT to compare them with SCIAMACHY measurements made at around 22:00 LT. Atmospheric density and temperature profiles provided by SABER were used in the [O] retrieval as discussed in Sect. 5. The concentrations of [O_2] and [N_2] were calculated from atmospheric density profiles assuming constant mixing ratios. The atomic oxygen mixing ratio profiles based on SABER measurements were converted into [O] profiles and used as reference [O] profiles for the verification of the retrieved [O] profiles (see Sect. 7).

2.3 MSIS and WACCM models

The Mass Spectrometer Incoherent Scatter semi-empirical atmospheric model (NRLMSISE-00) includes ground-based, rocket and satellite borne measurements. A set of parametric equations of diffusive equilibrium (Akins et al., 2003) is used to interpolate or extrapolate the data to complete them. Heliogeophysical conditions which influence the parameters relevant for the photochemical model were employed for the [O] retrieval in our study. These parameters, F10.7 (10.7 cm solar radio flux) and Ap-index (planetary equivalent daily amplitude) were taken from databases provided by National Oceanic and Atmospheric Administration (NOAA, 2014a). The NRLMSISE-00 model provided via the Internet (NRLMSISE-00, 2014) was used to simulate the concentration profiles of individual atmospheric constituents (i.e., [O], [O_2], [N_2]) and temperature profiles for the specifically chosen heliogeophysical conditions and geographical locations at 22:00 LT with 1.0 km altitude grid resolution.

In this study we also use atomic oxygen and atmospheric background parameters modelled with the Whole Atmosphere Community Climate Model (version 4) with specified dynamics (SD-WACCM4; see Garcia et al. (2007) for a description of a previous version of the model). SD-WACCM4 is nudged to GEOS-5 meteorological fields below about 50 km altitude. The SD-WACCM4 data set used in this study covers the period from April 2010 to March 2011 and was previously also employed by Hoffmann et al. (2012) and Kowalewski et al. (2014). The geopotential height profiles provided by SD-WACCM4 were converted to geometrical height profiles. Temperature profiles,

AMTD
7, 10829–10881, 2014

atmospheric pressure profiles and [O] profiles were interpolated from the geometrical height grid to an altitude grid with 1.0 km resolution. The $[O_2]$ and $[N_2]$ profiles required for the present study were calculated from SD-WACCM4 pressure and temperature profiles assuming the ideal gas law and constant $[O_2]$ and $[N_2]$ mixing ratios. As described by Kowalewski et al. (2014), we exploited the longitudinal variation of the SD-WACCM4 fields – provided with daily resolution at 00:00 UTC – to extract the required atmospheric parameters at 22:00 LT.

3 Determination of green line limb emission profiles

The nightglow limb spectral measurements provided by SCIAMACHY were screened and measurements from certain orbits were excluded according to measurement errors presented in the SOST-DLR quality and anomaly reports (SOST-DLR, 2013a, b, c, 2012, see Sect. 2.1).

The geographical position and extent of the air volumes observed by SCIAMACHY nighttime limb measurements on a single day are presented in Fig. 1. The duration of a single measurement is about 60 s and the horizontal resolution is about 1000 km × 630 km. The geographical positions of all nighttime limb measurements performed during the period from 2 August 2002 to 8 April 2012 are shown in Fig. 2. The measurements within the South Atlantic Anomaly (SAA) are shown in green in Fig. 2.

The measured spectra within the tangent height range from 75 to 128 km with 3.3 km vertical sampling were interpolated to 1.0 km altitude grid resolution within the spectral range 555–561 nm. For each individual spectrum the emission spectra averaged over the 110–126 km tangent height range were subtracted from the spectrum at each tangent height. Then each spectrum was separated into three parts corresponding to the following wavelength intervals: from 555 to 557 nm (background emissions and noise), from 557 to 559 nm (green line emission) and from 559 to 561 nm (background emissions and noise) (see Fig. 3). The spectral baseline underneath the green line was determined using the background and noise intervals and was subtracted from the

AMTD
7, 10829–10881, 2014

spectral data in the green line interval. Each individual spectrum was analysed with help of a band pass filter based on the application of variance and mean value thresholds within the wavelength intervals from 555 to 557 nm and from 559 to 561 nm. Measurement noise detection based on the variance threshold only was applied within the wavelength interval from 557 to 559 nm. The empirical choice and application of the threshold values are discussed below.

Envisat, as it passes through the South Atlantic Anomaly (SAA) at an altitude of approximately 800 km is exposed to high-energy particles within the lowest of the three Van Allen belts. The varying solar activity (Hudson et al., 2008) and solar coronal mass ejections (CMEs), like, e.g., the Halloween event in 2003 caused measurement interruptions (reported by SOST-DLR in data quality and anomaly reports, see Sect. 2.1). Spectra were excluded from the retrieval if the variance within the background wavelength intervals exceeded the variance threshold value of 50×10^6 Rayleigh^2 nm^{-2} (1 Rayleigh equals 10^{10} photon s^{-1} m^{-2}).

The geographical position of limb spectral measurements was used to exclude them from further processing in the case when contamination by aurora events was expected. The size of the aurora oval (Newell et al., 2002) varies constantly with each minute depending on the hemispheric power index provided by NOAA (2014b) that was used as a measure of the auroral activity in this study. The shape of the aurora oval was approximated with a circle centered at the north geomagnetic pole (80° N, 72° W) according to the International Geomagnetic Reference Field (IGRF-11) model. The area of such a circle is supposed to vary according to the value of the hemispheric power index so that spectra measured at geographical locations within this circle were excluded from daily and monthly averaging. In addition to this aurora position filter the variance threshold value of 60×10^6 Rayleigh^2 nm^{-2} was also applied within the green line wavelength interval to exclude non-valid spectral measurements.

The Q and P branch components of the OH(7-1) band emissions (Blackwell et al., 1960) can contribute to the green line emissions within the wavelength interval from 555 to 561 nm and so they should be considered. There are no other sources of nightglow

AMTD
7, 10829–10881, 2014

emissions contributing to the spectra of the analysed green line emissions to be additionally considered, except the one due to NO+O air afterglow reaction, which is – however – typically at least two orders of magnitude weaker than the O(^{1}S) green line (von Savigny et al., 1999). These contaminating emissions may affect the spectral baseline. The spectra were excluded from the retrieval if the absolute mean value in the background wavelength intervals exceeded the threshold value of 500 Rayleigh nm^{-1}. Figure 3 presents sample daily and monthly averaged spectra at 95 km altitude within the latitude range 20–25° N. Each spectral measurement processed was integrated over the green line wavelength interval from 557 to 559 nm. The green line limb emission rate (LER) profiles were daily or monthly averaged and converted to Rayleigh. Zonal averaging in 5° latitude bins was applied additionally because the zonal atmospheric motion in the MLT is much faster than the meridional motion. Daily and monthly averaged sample LER profiles within the latitude range 20–25° N are presented in Fig. 4.

4 Retrieval of volume emission rate profiles

The main task of this step of the retrieval procedure is to invert limb emission rate (LER) profiles (being a function of tangent height h) to vertical volume emission rate (VER) profiles (as a function of geometric altitude z), given that the elements of the LER profiles are integrals of the VER along the line of sight (LOS). The Earth's atmosphere, represented by the flattened Earth model WGS84 (e.g., NIMA, 2000; Larson and Wertz, 1999) is assumed to be composed of homogeneously emitting layers of 1 km thickness. The geometrical distances (optical paths) along the LOS passing through subsequent layers of the model atmosphere were calculated using the Pythagorean theorem.

The linear forward model (Rodgers, 2000) maps volume emission rate profiles from their state space into measurement space of limb emission rate profiles. Note that extinction due to scattering and self-absorption is negligible for this specific application.

AMTD
7, 10829–10881, 2014

The forward model is mathematically represented by the following linear relationship:

$$\boldsymbol{y} = \mathbf{F}(\boldsymbol{x}, \boldsymbol{b}) + \epsilon = \mathbf{K}\boldsymbol{x} + \epsilon \quad (1)$$

with LER profiles represented by the measurement vector $\boldsymbol{y}$, VER profiles represented by the state vector $\boldsymbol{x}$, $\mathbf{F}$ being the functional representation of the forward model, $\boldsymbol{b}$ representing errors in tangent height registration, and ϵ being a statistical uncertainty that includes both the uncertainty in $\boldsymbol{y}$ and in the elements of the weighting function matrix $\mathbf{K}$ (see Sect. 6). The inverse problem is even-determined for the chosen retrieval altitude grid resolution of 1.0 km being the same for the standard tangent height grid resolution.

A least squares method approach was employed to solve the inverse problem, minimizing the prediction error assuming linear system inconsistencies due to noise in $\boldsymbol{y}$. Phillips–Tikhonov regularization was chosen to avoid physically meaningless solutions such as oscillations due to, e.g., numerical sensitivity of the inversion.

The determination of SCIAMACHY tangent heights is characterized by uncertainties, but the tangent height error drift is with less than 20 m year^{-1} very small (Bramstedt, 2012). Because the resulting tangent height uncertainties affect the weighting function matrix $\mathbf{K}$, the total least squares method with regularization was applied to reduce potential numerical instabilities and oscillations due to uncertainties in $\boldsymbol{y}$ and $\mathbf{K}$.

At first, an inversion was performed using a constrained least squares approach:

$$\boldsymbol{x} = (\mathbf{K}^{\mathrm{T}}\mathbf{K} + \gamma_{\mathrm{r}}\mathbf{H}^{\mathrm{T}}\mathbf{H})^{-1}\mathbf{K}^{\mathrm{T}}\boldsymbol{y} = \mathbf{G}_{\mathrm{r}}\boldsymbol{y} \quad (2)$$

with the positive semi-definite regularization matrix $\mathbf{H}$ (Wang and Yuan, 2003) scaled with the regularization parameter γ_{r} (lower index r means "restricted", i.e., without considering $\mathbf{S}_{\mathrm{e}}$ and $\mathbf{S}_{\mathrm{a}}$), and the restricted gain matrix $\mathbf{G}_{\mathrm{r}}$ (also known as the generalised inverse matrix). To determine the value of γ_{r} the automated regularized total least squares (RTLS) procedure (see Sect. 4.2) was applied.

At the next step, the diagonal noise covariance matrix $\mathbf{S}_{\mathrm{e}}$ (corresponding to the 1 σ error of the current LER profile $\boldsymbol{y}$) was introduced. Uncertainty information of measured

AMTD
7, 10829–10881, 2014

LER profiles represented by $\mathbf{S}_e$ needs to be appropriately balanced with the a priori covariance matrix $\mathbf{S}_a$ related to retrieved target VER profiles $\boldsymbol{x}$. The first-order linear Bayesian approach (Rodgers, 2000) was implemented to solve Eq. (3) extended with $\mathbf{S}_e$ and $\mathbf{S}_a$ (see Sect. 4.1).

4.1 Implementation of the inversion procedure

The maximum a posteriori solution obtained after generalisation for independent components of the state vector $\boldsymbol{x}$ (Rodgers, 2000) is given by:

$$\boldsymbol{x} = \mathbf{S}_a\mathbf{K}^T(\mathbf{K}\mathbf{S}_a\mathbf{K}^T + \mathbf{S}_e + \gamma\mathbf{H}^T\mathbf{H})^{-1}\boldsymbol{y} = \mathbf{G}\boldsymbol{y} \quad (3)$$

with the positive semi-definite regularization matrix $\mathbf{H}$ (Wang and Yuan, 2003) scaled with the regularization parameter γ and the retrieval gain matrix $\mathbf{G}$. The inversion procedure becomes insensitive to the application of covariance matrices in the case of the a priori matrix $\mathbf{S}_a$ calculated with help of the $\mathbf{S}_e$ matrix.

Under the assumption (based on the fact of similarities in statistical distributions of $\mathbf{S}_a$ and $\mathbf{S}_e$ for our case) that $\mathbf{S}_a$ is calculated from $\mathbf{S}_e$, Eq. (3) gives us:

$$\overline{\mathrm{diag}(\mathbf{K}\mathbf{S}_a\mathbf{K}^T)} \approx \overline{\mathrm{diag}(\mathbf{S}_e)}. \quad (4)$$

A comparison of Eq. (2) and Eq. (3) gives that γ, γ_r and $\mathbf{S}_a$ are related as follows:

$$\gamma = \gamma_r \cdot \overline{\mathrm{diag}(\mathbf{S}_a)}. \quad (5)$$

Once γ_r is determined (see Eq. 2) using the RTLS procedure (see Sect. 4.2), γ can be calculated.

The presented γ calculation procedure is supported by evident equivalency of the VER profiles retrieved according to Eq. (2) (optimized for using γ_r) and Eq. (3) (optimized for using γ). The calculation procedure is supported also by the fact that the measurement vector $\boldsymbol{y}$ is similar to the synthetic vector $\boldsymbol{s} = \mathbf{K}\boldsymbol{x}$. Figure 5 presents the

AMTD
7, 10829–10881, 2014

results for LER profiles ($\boldsymbol{y}$) and synthetic profiles averaged for a sample day (Fig. 5a) and a sample month (Fig. 5d). Figure 6 presents sample daily and monthly averaged VER profiles ($\boldsymbol{x}$) within the latitude range 20–25° N.

The shape of the averaging kernel represented by a row of the matrix $\mathbf{A} = \mathbf{GK}$ is expected to be a simple peak (Rodgers, 1990). The area of the averaging kernels is defined by

$$a(z) = \int \mathbf{A}(z, z')\mathrm{d}z', \tag{6}$$

where z is the nominal altitude of the peak of the related averaging kernel. It characterizes the measurement response as a measure of the relative contribution of the observations and the a priori information corresponding to a retrieved VER profile (Rodgers, 2000). Figure 5 presents the averaging kernel rows (coloured lines) and the measurement response (red dashed line) for a sample day (Fig. 5b) and a sample month (Fig. 5e) for the 20–25° N latitude range. The area of the averaging kernels – characterizing the measurement response – is close to 1 within the altitude range from 86 to 122 km with some deviations at the edges of this altitude range.

The vertical resolution of the retrieved VER profiles (usually defined as the "width" of the averaging kernels) was evaluated using the Backus–Gilbert spread $r(z)$ that characterizes the prevalence of useful information against noise at the geometric altitude z (Rodgers, 1990):

$$r(z) = \frac{12}{a(z)^2} \int (z - z')^2 \mathbf{A}(z, z')^2 \mathrm{d}z'. \tag{7}$$

Figure 5 shows the vertical resolution according to Backus–Gilbert spread for a sample day (Fig. 5c) and a sample month (Fig. 5f) within the latitude range 20–25° N. The approximately 3.7 km vertical resolution of the retrieved VER profiles is slightly bigger than the vertical sampling of the measured LER profiles of approximately 3.3 km.

AMTD
7, 10829–10881, 2014

4.2 Regularized total least squares minimization

The automated regularized total least squares (RTLS) procedure (Sima et al., 2004) was applied to determine the value of the regularization parameter γ_r (see Eq. 5).

Partial solutions $\boldsymbol{x}_i$ of the regularized problem are calculated as a function of a fixed γ_r:

$$\boldsymbol{x}_i = (\mathbf{K}_{-i}^T \mathbf{K}_{-i} + \gamma_r \mathbf{H}^T \mathbf{H})^{-1} \mathbf{K}_{-i}^T \boldsymbol{y}_{-i} = \mathbf{G}_{CV} \boldsymbol{y}_{-i} \quad (8)$$

with $\mathbf{K}_{-i}$ being matrix $\mathbf{K}$ with rows i set to zero and $\boldsymbol{y}_{-i}$ being a measurement vector with elements i set to zero (Sima et al., 2004). The fitting bias associated with ignoring parts of the data is measured on the basis of the calculated set of $\boldsymbol{x}_i(\gamma_r)$ using the orthogonal distances composing the cross-validation (CV) function:

$$\mathrm{CV} = \sum_{i=1}^{N} \frac{\|\mathbf{K}_{-i} \boldsymbol{x}_i - \boldsymbol{y}_{-i}\|^2}{\|\boldsymbol{x}_i\|^2 + 1} \quad (9)$$

with $\mathbf{G}_{CV}$ being retrieval gain matrix corresponding to the CV function. The optimal γ_r is found at the minimum of the CV function (Sima et al., 2004). The RTLS algorithm was implemented with the LAPACK functions LUDC, LUSOL and LUMPROVE used in Interactive Data Language (IDL) version 8.2 to solve the reduced inversion equation (see Eq. 2).

The range of possible regularization parameters was selected empirically to speed up the process of the γ_r calculation. The range not shaded with blue colour in Fig. 7 represents the acceptable range of possible regularization parameters (in this Fig. the violet line corresponds to the CV function, the red line to the derivative of the CV function with respect to the index and the blue line to the regularization parameter function). Instabilities due to numerical random errors are present in the left part of CV function curve where the value of the regularization parameter γ_r is too small and the retrieval is under-regularized (see the blue-shaded zone on the left in Fig. 7). Small

AMTD
7, 10829–10881, 2014

values of regularization parameters cause roughness of the curve representing the retrieved state vector $\boldsymbol{x}$. Too high values of the regularization parameter result in spikes of the inversion error curve corresponding to the scaled norm-function $\|\mathbf{G}_{CV}^{-1}\mathbf{G}_{CV} - \mathbf{I}\|$ (see the black line in the blue-shaded zone on the right in Fig. 7). High values of regularization parameters mean overregularization and cause flatness of the retrieved state vector $\boldsymbol{x}$ curve.

The optimal γ_r is found automatically within the acceptable (not shaded) range. Within the acceptable range of γ_r the minimum of the CV function curve is identified to determine the optimal γ_r. If the minimum of the CV function is located beyond the acceptable range, the steepest slope of the CV function is identified using the derivative of the CV function.

4.3 Retrieval errors due to inversion

The retrieval error is characterized by the total retrieval error $\mathbf{S}_{tot}$ (Rodgers, 2000) estimated for the retrieved volume emission rate (VER) profiles (see Eq. 3) as follows:

$$\mathbf{S}_{tot} = \mathbf{S}_m + \mathbf{S}_s + \mathbf{S}_b + \mathbf{S}_f \quad (10)$$

with the measurement error covariance matrix $\mathbf{S}_m$ related to random and systematic errors and the smoothing error covariance matrix $\mathbf{S}_s$. The forward model parameter error is represented by covariance matrix $\mathbf{S}_f$ related to systematic errors and the error covariance matrix $\mathbf{S}_b$ represents random errors of model parameters that are not retrieved (see Sects. 4 and 6).

The covariance matrix $\mathbf{S}_m$ due to retrieval system noise is given by

$$\mathbf{S}_m = \mathbf{G}\mathbf{S}_e\mathbf{G}^T \quad (11)$$

with the retrieval gain matrix $\mathbf{G}$ (see Eq. 3):

$$\mathbf{G} = \mathbf{S}_a\mathbf{K}^T(\mathbf{K}\mathbf{S}_a\mathbf{K}^T + \mathbf{S}_e + \gamma\mathbf{H}^T\mathbf{H})^{-1}. \quad (12)$$

AMTD
7, 10829–10881, 2014

The covariance matrix $\mathbf{S}_s$ due to smoothing error is given by

$$\mathbf{S}_s = (\mathbf{A} - \mathbf{I})\mathbf{S}_n(\mathbf{A} - \mathbf{I})^T \quad (13)$$

with averaging kernel matrix $\mathbf{A} = \mathbf{GK}$, the identity matrix $\mathbf{I}$ and covariance matrix of the states' ensemble $\mathbf{S}_n$ about the mean state $\overline{\boldsymbol{x}}$ (Rodgers, 2000): $\mathbf{S}_n = \mathbf{E}[(\boldsymbol{x} - \overline{\boldsymbol{x}}) \cdot (\boldsymbol{x} - \overline{\boldsymbol{x}})^T]$.

The diagonal matrix $\mathbf{S}_b$ is the error covariance matrix containing the inverse and squared standard deviation (SD) of VER profiles with respect to uncertainties in the model parameters. The SD was found as the difference of the averaged VER profiles due to perturbations of h' representing the uncertainty in the tangent height determination (±500 m, see Sect. 6.1). The covariance matrix $\mathbf{S}_f$ due to forward model errors caused by approximations and imperfections of the forward model is given by

$$\mathbf{S}_f = \mathbf{GKS}_b\mathbf{K}^T\mathbf{G}^T. \quad (14)$$

5 Retrieval of atomic oxygen concentration profiles

The retrieval of atomic oxygen concentration ([O]) profiles from the obtained green line volume emission rate (VER) profiles is based on the generally accepted 2-step Barth transfer scheme and approximations derived from the measurements provided by the ETON rocket campaign (McDade et al., 1986). The $O(^1S–^1D)$ SCIAMACHY nightglow green line emission spectra were processed according to the retrieval approach presented in Sect. 4 resulting in the retrieved VER profiles. The [O] retrieval is based on the well known cubic equation (McDade et al., 1986), which represents the empirically derived relation between VER and [O] profiles, see Eq. (15).

The 2-step Barth transfer scheme is represented by chemical reactions (see Reactions 1, 2 and the resulting Reaction 10 for the green line emission in Table 1) accompanied by quenching. The quenching of O_2^* as well as the quenching of $O(^1S_0)$ by O_2 was considered by McDade et al. (1986). In addition, Gobbi et al. (1992), Semenov (1997), Semenov and Shefov (2005) and Khomich et al. (2008) also considered quenching

AMTD
7, 10829–10881, 2014

of $O(^1S_0)$ by $O(^3P)$ or N_2. The simplest of the [O] retrieval approaches based on the cubic equation does not account for the quenching of $O(^1S_0)$ by $O(^3P)$ or N_2, and the retrieved [O] profiles using such an approach are denoted as $[O^{cubic}]$. The [O] retrieval approach based on the extended cubic equation accounts the quenching of $O(^1S)$ by $O(^3P)$ or N_2, and the retrieved [O] profiles using such an approach are denoted as $[O^{quench}]$.

According to the differences of these model approaches the following equation based on the coefficients represented in Table 2 was used in the [O] retrieval:

$$\mathrm{VER} = \kappa_1[\mathrm{O}]^2([\mathrm{N_2}] + [\mathrm{O_2}]) \cdot \frac{[\mathrm{O}]}{(\mathrm{C}(0) + \mathrm{C}(1)[\mathrm{O}] + \mathrm{C}(2)[\mathrm{O_2}])} \cdot \frac{A_{558}}{(A_{1\mathrm{S}} + \sum_i ({}^i\kappa_5[M_i]))} \quad (15)$$

with A_{558} (s^{-1}) being the transition probability of $O(^1S–^1D)$, A_{1S} (s^{-1}) the inverse radiative lifetime of $O(^1S)$, κ_1 ($cm^3\,s^{-1}$) the rate coefficient for the three body recombination of atomic oxygen, ${}^i\kappa_5$ ($cm^3\,s^{-1}$) the rate coefficient for quenching of $O(^1S)$ by M_i, $i = 1,2,3$. The dimensionless variables C(0), C(1) and C(2) are the empirical $O(^1S)$ excitation parameters, $[M_i]$=([O], $[N_2]$, $[O_2]$) being concentrations of the respective species, $i = 1,2,3$.

The first term on the right-hand side of the Eq. (15) describes rate of O_2^* production, the first and second term the production of $O(^1S)$ and all three terms on right-hand side – the $^1S–^1D$ emission rate. Recombination of ground state atomic oxygen with rate κ_1 causes production of metastable oxygen O_2^*. Subsequent deactivation of O_2^* by ground state O leads to $O(^1S)$ production. Metastable molecular oxygen undergoes quenching described by parameters C(1), C(2) and radiative relaxation described by radiative lifetime $C(0)^{-1}$ so that the second term on the right-hand side of the Eq. (15) represents conversion to $O(^1S)$. The influence of $[O_2]$ and $[N_2]$ was accounted for by the approximated parameters C(0), C(1) and C(2) (McDade et al., 1986). The quenching of $O(^1S)$ by $O(^3P)$ or N_2 (described by reactions 7 and 8 in Table 1 and introduced by

AMTD
7, 10829–10881, 2014

Gobbi et al., 1992; Semenov, 1997; Semenov and Shefov, 2005; Khomich et al., 2008) is considered in the third term on the right-hand side of the Eq. (15).

The numerical approximation employed by Semenov (1997), Semenov and Shefov (2005) and Khomich et al. (2008) was applied to find the solution of Eq. (15) for ${}^{i}\kappa_5 \neq 0$, $i = 1,2,3$ that corresponds to retrieving $[O^{quench}]$ profiles. The atomic oxygen concentration $[O^{cubic}]$ was retrieved as the exact solution of the cubic equation resulting from the Eq. (15) for ${}^{1}\kappa_5 = {}^{2}\kappa_5 = 0$.

The discussed model approaches to retrieve [O] profiles according to Eq. (15) require parameters such as SCIAMACHY VER profiles, temperature dependent rate coefficients κ and atmospheric density ($[N_2] + [O_2]$) profiles. Both $[O^{quench}]$ and $[O^{cubic}]$ retrievals were performed for all available sources of temperature and atmospheric density profiles.

In an ideal case, simultaneous measurements of all quantities required to calculate atomic oxygen profiles (i.e., temperature (T), $[N_2]$, $[O_2]$ and VER profiles) are available. Unfortunately, such a data set is not available. So, in our case, the available SCIAMACHY VER profiles were combined with T, $[O_2]$, $[N_2]$ profiles from NRLMSISE-00, SD-WACCM4 and SABER to calculate $[O^{quench}]$ and $[O^{cubic}]$ profiles according to Eq. (15). The presented retrievals $[O^{cubic}]$ and $[O^{quench}]$ are in the following discussion additionally denoted with lower indices showing the source of the T, $[O_2]$ and $[N_2]$ profile data as $[O^{cubic}_{MSIS00}]$, $[O^{cubic}_{WACCM4}]$, $[O^{cubic}_{SABER}]$ and $[O^{quench}_{MSIS00}]$, $[O^{quench}_{WACCM4}]$, $[O^{quench}_{SABER}]$. The retrieved [O] profiles were compared with atomic oxygen concentration profiles extracted from NRLMSISE-00, SD-WACCM4 and SABER denoted as $[O^{MSIS00}]$, $[O^{WACCM4}]$, $[O^{SABER}]$, respectively. Figure 8 shows sample daily and monthly averaged $[O^{quench}_{SABER}]$ profiles within the latitude range 20–25° N.

AMTD
7, 10829–10881, 2014

6 Error analysis

The error analysis was done assuming independent contributions of uncertainty components to the maximum uncertainty of the retrieved data set, so correlations of the uncertainty components were neglected. The uncertainty components to be considered are assumed, first of all, to include random errors and systematic errors. The model parameters (that are not retrieved and related to random errors) correspond to the vector $\boldsymbol{b}$ (see Sect. 4). The components of the vector $\boldsymbol{b}$ are discussed at the relevant steps of the retrieval considering:

1. the error in the determination of the tangent height information affecting the VER retrieval (see Sect. 6.1),

2. the error in atmospheric density (represented by the sum of molecular oxygen [O_2] and nitrogen [N_2] concentrations) and temperature profiles affecting the [O] retrieval (see Sect. 6.2).

Successive addition of the uncertainty components to the solution was performed at each step of the retrieval. These steps result in (1) the spectral data set (P), (2) limb emission rate (LER) profiles, (3) volume emission rate (VER) and (4) atomic oxygen concentration [O] profiles. The error bounds (denoted by ±1) were estimated in a way to avoid assumptions about certain, e.g., normal, type of the parameter distributions.

At each step of the retrieval the relevant uncertainty components were accounted for (Kennedy et al., 2011) resulting in the error-free retrieval values ($\boldsymbol{P}_0 \Rightarrow \boldsymbol{LER}_0 \Rightarrow \boldsymbol{VER}_0 \Rightarrow [\boldsymbol{O}]_0$) and their upper and lower bounds ($\boldsymbol{P}_{+1} \Rightarrow \boldsymbol{LER}_{+1} \Rightarrow \boldsymbol{VER}_{+1} \Rightarrow [\boldsymbol{O}]_{+1}$ and $\boldsymbol{P}_{-1} \Rightarrow \boldsymbol{LER}_{-1} \Rightarrow \boldsymbol{VER}_{-1} \Rightarrow [\boldsymbol{O}]_{-1}$). The uncertainty components considered at a given step of the retrieval were taken into account for the error bounds at the next step of the retrieval.

AMTD
7, 10829–10881, 2014

6.1 Error analysis for the retrieval of volume emission rate profiles

The maximum tangent height (h) error of the SCIAMACHY limb measurements is assumed to be ±500 m ($h' = 500$ m) (von Savigny et al., 2009). Modelled in a discrete mode (by applying $\pm h'$) perturbations of h were considered to resemble the random error of the determination of the tangent height. The uncertainty of the measured spectrum $\boldsymbol{P}$ is composed of two additive altitude dependent components caused by variations of h (related to a random error vector $\boldsymbol{\sigma}_h$) and radiometric accuracy (related to a systematic error vector $\boldsymbol{\sigma}_a$). The altitude dependent vector of SDs $\boldsymbol{\sigma}_h$ was calculated using spectra $\boldsymbol{P}$ and perturbed spectra denoted as $\boldsymbol{P}^{\text{temp}}$: $\boldsymbol{\sigma}_h^+ = |\boldsymbol{P}^{\text{temp}}(+h') - \boldsymbol{P}|$ and $\boldsymbol{\sigma}_h^- = |\boldsymbol{P} - \boldsymbol{P}^{\text{temp}}(-h')|$.

A radiometric accuracy of the SCIAMACHY spectral measurements of 4 % ($a = 4$ %) (Noël et al., 1998) was assumed to calculate the altitude dependent vector of SDs $\boldsymbol{\sigma}_a$ of the averaged spectra: $\boldsymbol{\sigma}_a^+ = |\boldsymbol{P}^{\text{temp}}(+a) - \boldsymbol{P}|$ and $\boldsymbol{\sigma}_a^- = |\boldsymbol{P} - \boldsymbol{P}^{\text{temp}}(-a)|$. Subtracting $(\boldsymbol{\sigma}_a^- + \boldsymbol{\sigma}_h^-)$ from $\boldsymbol{P}$ yields the lower bound of the ±1 error bar of spectral data; its upper bound $\boldsymbol{P}_{+1}$ is calculated as $\boldsymbol{P}_{+1} = \boldsymbol{P} + (\boldsymbol{\sigma}_a^+ + \boldsymbol{\sigma}_h^+)$. The unchanged retrieval spectrum $\boldsymbol{P}_0$ is equal to $\boldsymbol{P}$. Figure 3 presents sample daily (Fig. 3a) and monthly (Fig. 3b) averaged green line spectra at the altitude of 95 km within the latitude range 20–25° N.

Each spectral data set ($\boldsymbol{P}_{-1}$, $\boldsymbol{P}_0$ and $\boldsymbol{P}_{+1}$) was processed (see Sect. 3) separately to calculate the corresponding LER profiles denoted by upper index temp: $\boldsymbol{LER}_{-1}^{\text{temp}}$, $\boldsymbol{LER}_0^{\text{temp}}$ and $\boldsymbol{LER}_{+1}^{\text{temp}}$. The emission-free spectral intervals (see Sect. 3) of $\boldsymbol{P}_0$ were used to calculate the uncertainty component (related to the random error vector $\boldsymbol{\sigma}_I$) of the LER when integrating over the green line spectral interval. The altitude dependent vector of SDs $\boldsymbol{\sigma}_I$ of $\boldsymbol{LER}_0$ was subtracted from $\boldsymbol{LER}_{-1}^{\text{temp}}$ that results in the lower error bound $\boldsymbol{LER}_{-1}$. The upper bound is $\boldsymbol{LER}_{+1} = \boldsymbol{LER}_{+1}^{\text{temp}} + \boldsymbol{\sigma}_I$. The unchanged LER profile $\boldsymbol{LER}_0$ is equal to $\boldsymbol{LER}_0^{\text{temp}}$ taken without perturbations used to estimate the ±1 error bar of the LER data set. Figure 4 presents sample daily (Fig. 4a) and monthly (Fig. 4b)

AMTD
7, 10829–10881, 2014

averaged LER profiles within the latitude range 20–25° N with calculated uncertainty components at the current step of the $\boldsymbol{LER}_{+1}$ or $\boldsymbol{LER}_{-1}$ retrieval.

The inversion scheme described above and supported by RTLS was applied to $\boldsymbol{LER}_{-1}$, $\boldsymbol{LER}_0$ and $\boldsymbol{LER}_{+1}$ to calculate VER profiles denoted with the upper index temp: $\boldsymbol{VER}_{-1}^{\text{temp}}$, $\boldsymbol{VER}_0^{\text{temp}}$ and $\boldsymbol{VER}_{+1}^{\text{temp}}$. From the diagonal elements of the error covariance matrix $\mathbf{S}_{\text{tot}}$ (see Eq. 10, Sect. 4.3) square roots were taken, resulting in the altitude dependent vector of SDs $\boldsymbol{\sigma}_{\mathbf{S}_{\text{tot}}}$. The uncertainties $\boldsymbol{\sigma}_{\mathbf{S}_{\text{tot}}}$ of $\boldsymbol{VER}_0$ were subtracted from $\boldsymbol{VER}_{-1}^{\text{temp}}$, resulting in the lower error bound $\boldsymbol{VER}_{-1}$. The upper bound is $\boldsymbol{VER}_{+1} = \boldsymbol{VER}_{+1}^{\text{temp}} + \boldsymbol{\sigma}_{\mathbf{S}_{\text{tot}}}$. The unchanged VER profile $\boldsymbol{VER}_0$ is equal to $\boldsymbol{VER}_0^{\text{temp}}$. Figure 6 presents sample daily (Fig. 6a) and monthly (Fig. 6b) averaged VER profiles within the latitude range 20–25° N with calculated uncertainty components of $\boldsymbol{\sigma}_{\mathbf{S}_{\text{tot}}}$ at the current step of $\boldsymbol{VER}_{+1}$ or $\boldsymbol{VER}_{-1}$ retrieval.

6.2 Error analysis for the retrieval of atomic oxygen concentration profiles

The maximum and minimum values of photochemical parameters (see Eq. 15) were used to estimate the contribution of photochemical model errors to the error in retrieved [O] profiles. The range of coefficients and other parameters used in the photochemical model (see Eq. 15) to determine the ±1 error bar of the [O] profiles are presented in Table 2.

Each VER profile ($\boldsymbol{VER}_{-1}$, $\boldsymbol{VER}_0$ and $\boldsymbol{VER}_{+1}$) was processed (see Sect. 5) assuming that simultaneously varied photochemical parameters cause maximum uncertainty of [O] separately, yielding [O] profiles denoted with the upper index temp: $[\boldsymbol{O}]_{-1}^{\text{temp}}$, $[\boldsymbol{O}]_0^{\text{temp}}$ and $[\boldsymbol{O}]_{+1}^{\text{temp}}$.

Moreover, model parameters that affect the [O] retrieval, but are not retrieved are considered at this step, i.e. temperature and the sum of molecular oxygen [O_2] and nitrogen [N_2] concentrations. To determine the influence of temperature and [O_2] + [N_2] on the resulting random error, temperature was perturbed by $T' = 5\,\text{K}$ and [O_2] +

AMTD
7, 10829–10881, 2014

$[N_2]$ by $D' = 10\,\%$. The altitude dependent vector of SDs σ_T was determined as: $\sigma_T^+ = |[O(+T')]_0^{temp} - [O]_0^{temp}|$ and $\sigma_T^- = |[O]_0^{temp} - [O(-T')]_0^{temp}|$. The altitude dependent SDs σ_D in perturbations of D' were calculated as follows: $\sigma_D^- = |[O(-D')]_0^{temp} - [O]_0^{temp}|$ and $\sigma_D^+ = |[O]_0^{temp} - [O(+D')]_0^{temp}|$. The cumulative uncertainties due to perturbations in T' and D' contribute simultaneously to the ±1 error bar of [O] causing maximum uncertainty: $\sigma_{TD}^+ = \sigma_T^+ + \sigma_D^-$ and $\sigma_{TD}^- = \sigma_T^- + \sigma_D^+$.

The uncertainties σ_{TD}^- of $[O]_0^{temp}$ were subtracted from $[O]_{-1}^{temp}$, resulting in the lower error bound $[O]_{-1}$. The upper bound is $[O]_{+1} = [O]_{+1}^{temp} + \sigma_{TD}^+$. The unchanged [O] profile $[O]_0$ is equal to $[O]_0^{temp}$ taken without perturbations used to estimate the ±1 error bar of the retrieved [O] data set. Figure 8 shows sample daily and monthly averaged atomic oxygen concentration ($[O_{SABER}^{quench}]$) profiles within the latitude range 20–25° N.

7 Results and discussion

In this section we first present in Sect. 7.1 results of the error analysis introduced in the previous section, followed by a verification and first validation of the retrieved [O] profiles. The verification of the [O] retrieval compares retrieved [O] profiles with reference [O] profiles and ideally allows a well-founded choice between the cubic and the extended cubic equations and a selection of appropriate source of temperature and density profiles from the different available sources. The verification was carried out in several steps including comparisons of reference and retrieved [O] profiles for:

1. sample profiles (see Sect. 7.2),
2. fields of relative differences (see Sect. 7.3),
3. fields of correlation coefficients (see Sect. 7.4).

AMTD
7, 10829–10881, 2014

In Sect. 7.5 we present first results on seasonal [O] variations in the SCIAMACHY and the reference data sets and on the complete SCIAMACHY [O] data set covering the period from August 2002 to April 2012.

7.1 Results of error analysis

The calculated uncertainty components in the retrieved VER profiles are represented by $\boldsymbol{VER}_{+1}$ and $\boldsymbol{VER}_{-1}$ in Fig. 6 with daily Fig. 6a and monthly Fig. 6b averaging within the latitude range 20–25° N. The distribution of uncertainty components in the retrieved [O] profiles is presented in Fig. 8 with daily (Fig. 8a) and monthly (Fig. 8b) averaging within the same latitude range. The negligible smoothing error $\boldsymbol{\sigma}_{\mathbf{S}_s}$ presented in the daily averaged VER and [O] profiles confirms the correctness of the averaging kernel calculation. The retrieval noise $\boldsymbol{\sigma}_{\mathbf{S}_m}$ component is represented by relatively large coloured zones in Fig. 6 and in Fig. 8. However, the corresponding coloured zone is smaller in the monthly averaged profiles because of a larger number of averaged profiles. The modelling error $\boldsymbol{\sigma}_{\mathbf{S}_f}$ in VER and [O] profiles is relatively small compared to the total uncertainty $\boldsymbol{\sigma}_{\mathbf{S}_{tot}}$ associated with the inversion procedure.

The [O] profile error associated with temperature errors assumes the highest values within the altitude range where the [O] peak occurs. Similar behaviour, but to a lesser extent, is characteristic for the [O] profile uncertainty caused by errors in atmospheric density (the sum of $[O_2]$ and $[N_2]$).

7.2 Verification step 1

Figure 9 shows atomic oxygen concentration ($[O^{quench}_{SABER}]$) profiles and reference [O] profiles provided by SABER, NRLMSISE-00 and SD-WACCM4 for a sample day and month. The altitude dependence of $[O^{quench}_{SABER}]$ in comparison with $[O^{SABER}]$, $[O^{MSIS00}]$ and $[O^{WACCM4}]$ shows certain deviations in the altitude range from 82 to 87 km that correspond to low values of the measurement response displayed in Fig. 5. The retrieved

AMTD
7, 10829–10881, 2014

$[O^{quench}_{SABER}]$ profiles are characterized by much higher concentrations in comparison to $[O^{MSIS00}]$ and a bit higher ones in the case of $[O^{WACCM4}]$. The monthly averaged $[O^{quench}_{SABER}]$ and $[O^{SABER}]$ profiles are quite similar.

Figures 10 and 11 show results for both available models (according to the cubic and the extended cubic equation, see Eq. 15) of the [O] retrieval, respectively. The figures clearly show that the [O] profiles based on the extended cubic approach show systematically larger [O] than the cubic approach, as expected. One can also see that the [O] profiles ($[O^{cubic}]$ or $[O^{quench}]$) retrieved with different available sources of temperature and density profiles are quite similar. A comparison of Figs. 9, 10 and 11 indicates that the $[O^{quench}]$ profiles are in better agreement with the SABER [O] profile measurements than the $[O^{cubic}]$ profiles. These results suggest that the extended cubic equation is preferable. This finding is further substantiated by comparisons to a larger SABER data set in the following subsection.

7.3 Verification step 2

Relative differences were calculated according to the equation $\epsilon = ([O]^{retr.} - [O]^{ref.})/[O]^{ref.}$ within the time period from April 2010 to March 2011 because for this time period SD-WACCM4 data were available. Figure 12 presents sample distributions of relative [O] differences as a function of latitude and altitude. The comparison indicates that already the $[O^{cubic}_{MSIS00}]$ profiles exhibit significantly higher oxygen concentrations than the $[O^{MSIS00}]$ profiles. The relative differences of $[O^{quench}_{MSIS00}]$ vs. $[O^{MSIS00}]$ (not shown) are – as expected – even bigger than those ones of $[O^{cubic}_{MSIS00}]$ vs. $[O^{MSIS00}]$. A similar situation occurs for relative differences of $[O^{quench}_{WACCM4}]$ vs. $[O^{WACCM4}]$ (not shown), but to a slightly lesser extent. The relative differences of $[O^{quench}_{SABER}]$ vs. $[O^{SABER}]$ are the smallest, and in particular smaller than the differences between $[O^{cubic}_{SABER}]$ and $[O^{SABER}]$. Over a large range of latitudes and altitudes the agreement between $[O^{quench}_{SABER}]$

AMTD
7, 10829–10881, 2014

and [O^{SABER}] is within about 15 % and has to be considered very good. If we assume the SABER [O] retrievals to be the most reliable reference profile source – compared to NRLMSISE-00 and SD-WACCM4 – then our comparison results favor the extended cubic equation over the cubic equation.

We now briefly discuss differences between the O retrievals from SCIAMACHY O green line observations derived in this study with similar retrievals – also from SCIAMACHY O green line measurements – recently presented by Kaufmann et al. (2014). Kaufmann et al. (2014) also compared their retrievals to co-located SABER measurements and found an approximately 30 % low bias compared to SABER atomic oxygen. Since the photochemical model employed by Kaufmann et al. (2014) is essentially the one by McDade et al. (1986) – corresponding to our [O^{cubic}_{SABER}] data set (see lower left panel of Fig. 12) – the agreement between the Kaufmann et al. (2014) retrievals and the our retrievals is very good.

7.4 Verification step 3

A Pearson cross-correlation analysis between the retrieved and the reference [O] profiles was performed within the time period from April 2010 to March 2011. The calculated correlation coefficients were analysed using the Fischer t test. Figure 13 shows sample correlation coefficient fields as a function of latitude and altitude for monthly averaged (top row and bottom left panel), and daily averaged (bottom right panel) [O]. Regions with correlation coefficients significant at the 68 % confidence level are indicated by solid contour lines, while areas characterized by lower significance are characterized by dotted contour lines and missing contour labels.

The cross-correlation between SCIAMACHY and NLRMSISE-00 [O] profiles (top left panel in Fig. 13) indicates that there exists a phase shift of about 180° in the seasonal variations in the northern tropical region. In a recent study Sheese et al. (2011) reported on a similar 180° phase shift of [O^{MSIS00}] compared daytime OSIRIS [O] profile measurements. In addition, Russell et al. (2005) found a 180° phase shift in the tidal

AMTD
7, 10829–10881, 2014

signature in MSIS-90 [O] compared to WINDII [O] measurements and model simulations with the TIME-GCM model.

The correlation between SCIAMACHY ($[O^{quench}_{WACCM4}]$) and SD-WACCM $[O^{WACCM4}]$ profiles (top right panel) is characterized by relatively high correlation coefficients in large parts of the latitude/height ranges shown. Directly above the equator, the correlation is lower, particularly above the [O] peak.

The correlation coefficient field for monthly averaged $[O^{quench}_{SABER}]$ vs. $[O^{SABER}]$ does not contain the areas of negative (NRLMSISE-00) or extensive areas with low (SD-WACCM4) values that indicate discrepancies of the retrieved $[O^{quench}_{SABER}]$ compared to $[O^{MSIS00}]$ or $[O^{WACCM4}]$. The correlation of $[O^{quench}_{SABER}]$ with the SABER measurements on a daily basis (bottom right panel) shows a similar pattern than for the monthly averaged data, but with lower correlation coefficients, as expected. We note that both for the monthly and daily averaged data there appears an altitude range with relatively high correlation coefficients – between about 88 and 95 km. This may be related to the fact that the atomic oxygen profile retrievals from SABER and SCIAMACHY measurements are based on different airglow emissions that peak at different altitudes. The SABER night-time atomic oxygen profiles are retrieved from the Meinel band volume emission rate (OH^* near 2 µm) profiles, which peaks are at about 87 km. In contrast, the O green line emission used to retrieve atomic oxygen profiles from SCIAMACHY night-time measurements peak near 95 km. [O] profiles can only be retrieved well from the different airglow emissions at altitudes with non-negligible emission. We may therefore expect, that the SABER [O] profile retrievals become more and more inaccurate above about 95 km, and the SCIAMACHY become more inaccurate below about 87 km.

7.5 Seasonal variations

We now present some first sample results on the morphology of atomic oxygen in the MLT region. More detailed analyses of different aspects of the spatio-temporal variability of atomic oxygen will be the foci of future studies.

AMTD
7, 10829–10881, 2014

Figure 14 shows seasonal variations in vertically averaged (85–100 km) SD-WACCM4 (top left panel), SABER (top right panel) and SCIAMACHY (bottom left panel) atomic oxygen for the time period from April 2010 to March 2011, together with vertically averaged green line volume emission rates measured with SCIAMACHY (bottom right panel). When focusing at latitudes close to the equator all panels show a dominating semi-annual variation with maxima around the equinoxes. However, there are also differences. The enhanced atomic oxygen abundances seen in the SCIAMACHY data (bottom left panel) in boreal fall and winter at latitudes above 20° N – consistent with a similar enhancement in the volume emission rates (bottom left panel) – are not that apparent in the SD-WACCM and SABER data sets. The reason for this discrepancy is currently unknown. We note, however, that similar oxygen anomalies at about 20° N in March 2010 and September 2010 are found in SABER and SCIAMACHY atomic oxygen fields, but not in modelled [O^{WACCM4}].

Figure 15 shows contour plots of O green line volume emission rate (top row) and retrieved atomic oxygen (bottom row) as a function of time and altitude with monthly (left column) and daily (right column) resolution for the 10–20° N latitude range and for the entire SCIAMACHY mission period from August 2002 to April 2012. Note that in case of the results for daily averaging (Figs. 14 and 15), gaps in the SABER temperature data set were filled with monthly averaged temperature data. The measurement gaps indicated by white areas in Fig. 15 are a consequence of missing SCIAMACHY raw data during these periods. The volume emission rate as well as the O profile data presented in Fig. 15 show evidence for pronounced semi-annual – with the well established equinox maxima – and 11 year solar cycle signatures, with the solar cycle signature being more obvious at altitudes above about 95 km than below. An annual component is also visible associated with a major minimum in boreal winter and a minor minimum in boreal summer. These signatures are consistent with earlier studies, and will be the foci of future investigations of this comprehensive data set of atomic oxygen profiles in the MLT region.

AMTD
7, 10829–10881, 2014

8 Conclusions

Atomic oxygen concentration profiles in the MLT region were retrieved from SCIAMACHY observations of the O green line emission in the terrestrial nightglow. The inversion of integrated limb emission rate profiles to vertical emission rate profiles was performed with a linear least squares minimization technique with regularization. The employed photochemical model is based on the generally accepted 2-step Barth transfer scheme and [O] retrievals were carried out for the standard empirical photochemical model by McDade et al. (1986) as well as for an extended version that also considers quenching of $O(^1S_0)$ by $O(^3P)$ or N_2.

A comprehensive sensitivity analysis was carried out to determine the effect of various error contributions occurring at the different steps of the [O] profile retrieval including the effect of errors in tangent height registration, limited radiometric accuracy, the impact of measurement errors, parameter errors and smoothing errors. Using the sensitivity analysis results an error budget for the [O] profile retrievals from SCIAMACHY green line nightglow observations was established based on successive linear addition of the estimated uncertainty components in order to avoid any assumptions concerning distributions of model parameters and other error components.

The retrieved [O] profiles were compared to simulations with NRLMSISE-00 and SD-WACCM and observations with SABER. The comparisons showed that NRLMSISE-00 [O] concentrations are systematically lower than data from the three other sources. Moreover, the SCIAMACHY [O] profiles are in good agreement with co-located SABER observations, if the extended photochemical model – considering quenching of $O(^1S_0)$ by $O(^3P)$ or N_2 – is used. This is an indication, that the extended photochemical model is more appropriate for retrieving [O] profiles from the O green line emission than the standard photochemical model.

The implemented retrieval scheme was applied to the entire SCIAMACHY data set, covering the period from August 2002 to April 2012, providing one of the most comprehensive atomic oxygen data sets in the MLT region. This data set will be evaluated

AMTD
7, 10829–10881, 2014

in the near future to investigate seasonal, long-term, as well as solar cycle variations, both at the 11 year and 27 day temporal scale.

Appendix:

This appendix provides explanations for Table 2 showing upper and lower boundaries of the photochemical model parameters relevant for the retrieval of atomic oxygen profiles from O(^{1}S) green line airglow measurements (see Sect. 5). The maximum and minimum values of A_{558} were taken from the works of Nakayama et al. (2006) (1.26 s^{-1}) – also used by Gao et al. (2012) – and Snively et al. (2010) (1.06 s^{-1}), respectively. The A_{558} values used by McDade et al. (1986) (1.18 s^{-1}), Makhlouf et al. (1998) (1.18 s^{-1}), Semenov (1997) (1.215 s^{-1}) and Khomich et al. (2008) (1.215 s^{-1}) are between these maximum/minimum values.

The maximum and minimum values of A_{1S} were taken from McDade et al. (1986) (1.35 s^{-1}, based on research of Nicolaides et al., 1971) and Snively et al. (2010) (1.105 s^{-1}), respectively. The dimensionless values C(0), C(1) and C(2) correspond to the fitting coefficients C'^{O}/C'^{O_2}, C'^{O} and C'^{O_2} (see McDade et al., 1986), which represent quenching by the different species (the *used coefficients* typically correspond to multiple reactions represented by the *intermediate coefficients*; see Table 1). The maximum and minimum values of C(0), C(1) and C(2) used here were taken from McDade et al. (1986).

The rate coefficients are calculated in this study as follows:

$$\kappa_1 = k_1 \times 10^{-33} \cdot (300/T)^2,$$

$${}^1\kappa_5 = {}^1k_5 \times 10^{-11} \cdot e^{-305/T},$$

$${}^2\kappa_5 = {}^2k_5 \times 10^{-17} \text{ and}$$

$${}^3\kappa_5 = {}^3k_5 \times 10^{-12} \cdot e^{-(812-1.82\times10^{-3}\cdot T^2)/T}.$$

AMTD
7, 10829–10881, 2014

A value of $k_1 = 4.7$ was used for the standard retrieval and the temperature dependence of κ_1 was taken from McDade et al. (1986), as also done by Gao et al. (2012). The uncertainty range of k_1 (see Table 1) was estimated according to the uncertainties typical for the laboratory work performed by Campbell and Gray (1973). In terms of the temperature dependence of ${}^1\kappa_5$ we used the same expression as in Semenov (1997), Khomich et al. (2008) and von Savigny and Lednyts'kyy (2013). The uncertainty range of ${}^1k_5$ was taken from Slanger and Black (1976) and is also used by Witt et al. (1979). The value of ${}^2\kappa_5$ was taken from Okabe (1978) and it is used to calculate the maximum and minimum values by assuming a 10 % uncertainty. Gobbi et al. (1992) and Nakayama et al. (2006) also used a ${}^2\kappa_5$ value within 10 % of the Okabe (1978) value. The value of ${}^3k_5$, its uncertainty range and the temperature dependence of ${}^3\kappa_5$ was taken from Capetanakis et al. (1993), as was done by von Savigny and Lednyts'kyy (2013) as well.

Finally, we note that the temperature dependence of κ_1 and ${}^2\kappa_5$ was originally used by McDade et al. (1986) with temperature profiles provided by MSIS-83 atmospheric model.

Acknowledgements. This work was partly funded by Ernst-Moritz-Arndt-University of Greifswald. SCIAMACHY is jointly funded by Germany, the Netherlands and Belgium. SCIAMACHY Level 1 data was kindly provided by the European Space Agency (ESA). We are indebted to the SABER team and NASA for making SABER data available. The authors thank Ian C. McDade (York University, Toronto), Stefan Kowalewski (IUP Bremen) and Martin Kaufmann (Forschungszentrum Jülich) for helpful discussions.

References

Akins, K. A., Healy, L. M., Coffey, S. L., and Picone, J. M.: Comparison of MSIS and Jacchia atmospheric density models for orbit determination and propagation, proceedings of the 13th AAS/AIAA space flight mechanics meeting, Ponce, Puerto Rico, Adv. Astronaut. Sci., 114, 951–970, 2003. 10835

AMTD
7, 10829–10881, 2014

Blackwell, D. E., Ingham, M. F., and Rundle, H. N.: The night-sky spectrum $\lambda\lambda$ 5000–6500 A, Astrophys. J., 131, 15–24, doi:10.1086/146801, 1960. 10837, 10868

Bovensmann, H., Burrows, J. P. Buchwitz, M., Frerick, J., Noël, S., Rozanov, V. V., Chance, K. V., and Goede, A. P. H.: SCIAMACHY: mission objectives and measurement modes, J. Atmos. Sci., 2, 127–150, doi:10.1175/1520-0469(1999)056<0127:SMOAMM>2.0.CO;2, 1999. 10833

Bramstedt, K., Noël, S., Bovensmann, H., Gottwald, M., and Burrows, J. P.: Precise pointing knowledge for SCIAMACHY solar occultation measurements, Atmos. Meas. Tech., 5, 2867–2880, doi:10.5194/amt-5-2867-2012, 2012. 10839

Burrows, J. P., Hölzle, E., Goede, A. P. H., Visser, H., and Fricke, W.: SCIAMACHY – scanning imaging absorption spectrometer for atmospheric chartography, Acta Astronaut., 35, 445–451, doi:10.1016/0094-5765(94)00278-T, 1995. 10833

Campbell, I. M. and Gray, C. N.: Rate constants for O(^{3}P) recombination and association with N(^{4}S), Chem. Phys. Lett., 18, 607–609, 1973. 10858

Capetanakis, F. P., Sondermann, F., Höser, S., and Stuhl, F.: Temperature dependence of the quenching of O(1S) by simple inorganic molecules, J. Chem. Phys., 98, 7883, doi:10.1063/1.464596, 1993. 10858

Cardaci, M.: ENVISAT-1 products specifications, Vol. 15, SCIAMACHY Products Specifications, available at: http://earth.esa.int/pub/ESA_DOC/ENVISAT/Vol15_Sciamachy_3L_1.1.pdf (last access: 15 March 2014), 2010. 10834

Department of Defense World Geodetic System 1984, Its Definition and Relationships with Local Geodetic Systems, National Imagery and Mapping Agency, Technical report 8350.2, 2000, available at: http://earth-info.nga.mil/GandG/publications/tr8350.2/wgs84fin.pdf (last access: 15 March 2014), 2000. 10838

Egerton, A. C.: Lord Rayleigh, 1875–1947, Obit. Not. Fell. R. Soc., 6, 502–538, 1949. 10831

Gao, H., Nee, J.-B., and Xu, J.: The emission of oxygen green line and density of O atom determined by using ISUAL and SABER measurements, Ann. Geophys., 30, 695–701, doi:10.5194/angeo-30-695-2012, 2012. 10833, 10857, 10858

Garcia, R. R., Marsh, D. R., Kinnison, D. E., Boville, B. A., and Sassi, F.: Simulation of secular trends in the middle atmosphere, 1950–2003, J. Geophys. Res., 112, D09301, doi:10.1029/2006JD007485, 2007. 10835

AMTD
7, 10829–10881, 2014

Gobbi, D., Takahashi, H., Clemesha, B. R., and Batista, P. P.: Equatorial atomic oxygen profiles derived from rocket observations of OI 557.7 nm airglow emission, Planet. Space Sci., 40, 775–781, 1992. 10831, 10832, 10844, 10846, 10858, 10865, 10877

Gottwald, M., Bovensmann, H., Lichtenberg, G., Noël, S., von Bargen, A., Slijkhuis, S., Piters, A., Hoogeveen, R., von Savigny, C., Buchwitz, M., Kokhanovsky, A., Richter, A., Rozanov, A., Holzer-Popp, T., Bramstedt, K., Lambert, J.-C., Skupin, J., Wittrock, F., Schrijver, H., and Burrows, J. P.: SCIAMACHY, Monitoring the Changing Earth's Atmosphere, DLR, 2006. 10833

Hoffmann, C. G., Kinnison, D. E., Garcia, R. R., Palm, M., Notholt, J., Raffalski, U., and Hochschild, G.: CO at 40–80 km above Kiruna observed by the ground-based microwave radiometer KIMRA and simulated by the Whole Atmosphere Community Climate Model, Atmos. Chem. Phys., 12, 3261–3271, doi:10.5194/acp-12-3261-2012, 2012. 10835

Hudson, M. K., Kress, B. T., Mueller, H.-R., Zastrow, J. A., and Blake, J. B.: Relationship of the Van Allen radiation belts to solar wind drivers, J. Atmos. Sol.-Terr. Phys., 70, 708–729, doi:10.1016/j.jastp.2007.11.003, 2008. 10837

Iwagami, N., Shibaki, T., Suzuki, T., Sekiguchi, H., Takegawa, N., and Morrow, W. H.: Rocket observations of atomic oxygen density and airglow emission rate in the WAVE2000 campaign, J. Atmos. Sol.-Terr. Phys., 65, 1349–1360, doi:10.1016/j.jastp.2003.08.002, 2003. 10831

Jursa, A. S.: Handbook of Geophysics and Space Environment, Air Force Research Laboratory, Space Vehicles Directorate, Battlespace Environment Division, 4th Edn., available at: http://www.cnofs.org/Handbook_of_Geophysics_1985/pdf_menu.htm (last access: 15 March 2014), 1985. 10831

Kaiser, J. W., von Savigny, C., Eichmann, K.-U., Noël, S., Bovensmann, H., Frerick, J., Burrows, J. P.: Satellite-pointing retrieval from atmospheric limb-scattering of solar UV-B radiation, Can. J. Phys., 82, 1041–1052, doi:10.1139/p04-071, 2004. 10834

Kaufmann, M., Zhu, Y., Ern, M., and Riese, M.: Global distribution of atomic oxygen in the mesopause region as derived from SCIAMACHY O(^{1}S) green line measurements, Geophys. Res. Lett., 41, 6274–6280, doi:10.1002/2014GL060574, 2014. 10833, 10853

Kennedy, J. J., Rayner, N. A., Smith, R. O., Parker, D. E., and Saunby, M.: Reassessing biases and other uncertainties in sea-surface temperature observations measured in situ since 1850, part 2: biases and homogenisation J. Geophys. Res., 116, D14104, doi:10.1029/2010JD015220, 2011. 10832, 10847

AMTD
7, 10829–10881, 2014

Khomich, V. Y., Semenov, A. I., and Shefov, N. N.: Airglow as an Indicator of Upper Atmospheric Structure and Dynamics, Springer, 739 pp., 2008. 10832, 10844, 10846, 10857, 10858, 10865, 10877

Kita, K., Iwagami, K., and Ogawa, T.: Rocket observations of oxygen night airglows: excitation mechanisms and oxygen atom concentration, Planet. Space Sci., 40, 1269–1288, 1992. 10831

Kowalewski, S., von Savigny, C., Palm, M., McDade, I. C., and Notholt, J.: On the impact of the temporal variability of the collisional quenching process on the mesospheric OH emission layer: a study based on SD-WACCM4 and SABER, Atmos. Chem. Phys., 14, 10193–10210, doi:10.5194/acp-14-10193-2014, 2014. 10835, 10836

Larson, W. J. and Wertz, J. R.: Space Mission Analysis and Design, Microcosm Press and Kluwer Academic Publishers, 920 pp., 1999. 10838

Liu, H. L., Foster, B. T., Hagan, M. E., McInerney, J. M., Maute, A., Qian, L., Richmond, A. D., Roble, R. G., Solomon, S. C., Garcia, R. R., Kinnison, D., Marsh, D. R., Smith, A. K., Richter, J., Sassi, F., and Oberheide, J.: Thermosphere extension of the whole atmosphere community climate model, J. Geophys. Res., 115, A12302, doi:10.1029/2010JA015586, 2010. 10832

Makhlouf, U. B., Picard, R. H., Winick, J. R., and Tuan, T. F.: A model for the response of the atomic oxygen 557.7 nm and the OH Meinel airglow to atmospheric gravity waves in a realistic atmosphere, J. Geophys. Res., 103, 6261–6269, 1998. 10857

McDade, I. C., Murtagh, D. P., Greer, R. G. H., Dickinson, P. H. G., Witt, G., Stegman, J., Llewellyn, E. J., Thomas, L., and Jenkins, D. B.: ETON 2: Quenching parameters for the precursors of $O_2(b^1\sum_g^+)$ and $O(^1S)$ in the terrestrial nightglow, Planet. Space Sci., 34, 789–800, 1986. 10831, 10832, 10833, 10844, 10845, 10853, 10856, 10857, 10858, 10865, 10876

Melo, S. M. L., Takahashi, H., Clemesha, B. R., Batista, P. P., and Simonich, D. M.: Atomic oxygen concentrations from rocket airglow observations in the equatorial region, J. Atmos. Terr. Phys., 58, 1935–1942, 1996. 10831

Mertens, C. J., Russell, J. M., III, Mlynczak, M. G., She, C.-Y., Schmidlin, F. J., Goldberg, R. A., Lopez-Puertas, M., Wintersteiner, P. P., Picard, R. H., Winick, J. R., and Xu, X.: Kinetic temperature and carbon dioxide from broadband infrared limb emission measurements taken from the TIMED/SABER instrument, Adv. Space Res., 43, 15–27, doi:10.1016/j.asr.2008.04.017, 2009. 10834

AMTD
7, 10829–10881, 2014

Mlynczak, M. G. and Solomon, S.: A detailed evaluation of the heating efficiency in the middle atmosphere, J. Geophys. Res., 98, 10517–10541, doi:10.1029/93JD00315, 1993. 10831
Mlynczak, M. G., Hunt, L. H., Mast, J. C., Marshall, B. T., Russell III, J. M., Smith, A. K., Siskind, D. E., Yee, J.-H., Mertens, C. J., Martin-Torres, F. J., Thompson, R. E., Drob, D. P., and Gordley, L. L.: Atomic oxygen in the mesosphere and lower thermosphere derived from SABER: Algorithm theoretical basis and measurement uncertainty, J. Geophys. Res., 118, 5724–5735, doi:10.1002/jgrd.50401, 2013. 10834
Nakayama, T., Takahashi, K., Matsumi, Y., and Fujiwara, H.: Laboratory study of O(^{1}S) formation process in the photolysis of O_3 and its atmospheric implications, J. Atmos. Chem., 53, 107–122, doi:10.1007/s10874-006-0597-3, 2006. 10857, 10858
Newell, P. T., Sotirelis, T., Ruohoniemi, J. M., Carbary, J. F., Liou, K., Skura, J. P., Meng, C.-I., Deehr, C., Wilkinson, D., and Rich, F. J.: OVATION: Oval variation, assessment, tracking, intensity, and online nowcasting, Ann. Geophys., 20, 1039–1047, doi:10.5194/angeo-20-1039-2002, 2002. 10837
Nicolaides, C., Sinanoğlu, O., and Westhaus, P.: Theory of atomic structure including electron correlation. IV, Method for forbidden-transition probabilities with results for [O I], [O II], [O III], [N I], [N II] and [C I], Phys. Rev. A, 4, 1400–1410, doi:10.1103/PhysRevA.4.1400, 1971. 10857
NOAA: National Geophysical Data Center, Kp/Ap dataset, available at: ftp://ftp.ngdc.noaa.gov/STP/GEOMAGNETIC_DATA/INDICES/KP_AP/ (last access: 15 March 2014), 2014a. 10835
NOAA: Hemispheric Power Data lists, available at: http://www.swpc.noaa.gov/ftpdir/lists/hpi/ (last access: 15 March 2014), 2014b. 10837
Noël, S., Bovensmann, H., Burrows, J. P., Frerick, J., Chance, K. V., Goede, A. H. P., and Muller, C.: The SCIAMACHY instrument on ENVISAT-1, in: Sensors, Systems, and Next-Generation Satellites II, Vol. 3498 of Proc. SPIE, edited by: Fujisada, H., 94–104, 1998. 10848
NRLMSISE-00: Atmosphere Model, available at: http://ccmc.gsfc.nasa.gov/modelweb/models/nrlmsise00.php (last access: 15 March 2014), 2014. 10835
Okabe, H.: Photochemistry of small molecules, A Wiley-Interscience publication, ISBN 0-471-65304-7, 1978. 10858
Picone, J. M., Hedin, A. E., Drob, D. P., and Aikin, A. C.: NRLMSISE-00 empirical model of the atmosphere: Statistical comparisons and scientific issues, J. Geophys. Res., 107, 1468, doi:10.1029/2002JA009430, 2002. 10832

AMTD
7, 10829–10881, 2014

Rodgers, C. D.: Characterization and error analysis of profiles retrieved from remote sounding measurements, J. Geophys. Res., 95, 5587–5595, 1990. 10841
Rodgers, C. D.: Inverse Methods for Atmospheric Sounding: Theory and Practice, Series on Atmospheric, Oceanic and Planetary Physics, Vol. 2, World Scientific Publishing, 2000. 10838, 10840, 10841, 10843, 10844
Russell III, J. M., Mlynczak, M. G., Gordley, L. L., Tansock, J., and Esplin, R.: An overview of the SABER experiment and preliminary calibration results, Proc. SPIE, 3756, 277–288, doi:10.1117/12.366382, 1999. 10832
Russell, J. P., Ward, W. E., Lowe, R. P., Roble, R. G., Shepherd, G. G., and Solheim, B.: Atomic oxygen profiles (80 to 115 km) derived from wind imaging interferometer/upper atmospheric research satellite measurements of the hydroxyl and greenline airglow: local time – latitude dependence, J. Geophys. Res., 110, D15305, doi:10.1029/2004JD005570, 2005. 10833, 10853
SABER: level 2A data (version 2.0), available at: http://saber.gats-inc.com/browse_data.php (last access: 15 March 2014), updated in 2014. 10834
Semenov, A. I.: Long-term changes in the height profiles of ozone and atomic oxygen in the lower thermosphere, Geomagn. Aeronomy+, 37, 354–360, 1997. 10832, 10844, 10846, 10857, 10858
Semenov, A. I. and Shefov, N. N.: Model of the vertical profile of the atomic oxygen concentration in the mesopause and lower ionosphere region, Geomagn. Aeronomy+, 45, 797–808, 2005. 10844, 10846
Sima, D. M., van Huffel, S., and Golub, G. H.: Regularized total least squares based on quadratic eigenvalue problem solvers, BIT, 44, 739–812, 2004. 10842
Sheese, P. E., McDade, I. C., Gattinger, R. L., and Llewellyn, E. J.: Atomic oxygen densities retrieved from optical spectrograph and infrared imaging system observations of O_2 A-band airglow emission in the mesosphere and lower thermosphere, J. Geophys. Res., 116, D01303, doi:10.1029/2010JD014640, 2011. 10833, 10853
Slanger, T. G. and Black, G.: O(^{1}S) production from oxygen atom recombination, J. Chem. Phys., 64, 3767, doi:10.1063/1.432692, 1976. 10858
Snively, J. B., Pasko, V. P., and Taylor, M. J.: OH and OI airglow layer modulation by ducted short-period gravity waves: effects of trapping altitude, J. Geophys. Res., 115, A11311, doi:10.1029/2009JA015236, 2010. 10857

AMTD
7, 10829–10881, 2014

SOST-DLR: Anomaly Reports, available at: http://www.atmos.caf.dlr.de/projects/scops/instrument_monitoring/anomaly_reports_actual.html (last access: 15 March 2014), updated on 10 May 2012. 10834, 10836

SOST-DLR, data quality – thermal performance, available at: http://www.atmos.caf.dlr.de/projects/scops/instrument_monitoring/data_quality_thermal.html (last access: 15 March 2014), updated on 30 January 2013a. 10834, 10836

SOST-DLR: data quality – pointing (2008–2012) performance, available at: http://www.atmos.caf.dlr.de/projects/scops/instrument_monitoring/data_quality_pointing_2008_2012.html (last access: 15 March 2014), updated on 31 January 2013b. 10834, 10836

SOST-DLR: Data quality – pointing (2002–2007) performance, available at: http://www.atmos.caf.dlr.de/projects/scops/instrument_monitoring/data_quality_pointing_2002_2007.html (last access: 15 March 2014), updated on 31 January 2013c. 10834, 10836

von Savigny, C. and Lednyts'kyy, O.: On the relationship between atomic oxygen and vertical shifts between OH Meinel bands originating from different vibrational levels, Geophys. Res. Lett., 40, 1–5, doi:10.1002/2013GL058017, 2013. 10858

von Savigny, C. H. A., McDade, I. C., Shepherd, G. G., and Rochon, Y.: Lower thermospheric nitric oxide concentrations derived from WINDII observations of the green nightglow continuum at 553.1 nm, Ann. Geophys., 17, 1439–1446, doi:10.1007/s00585-999-1439-9, 1999. 10838, 10868

von Savigny, C., Bovensmann, H., Bramstedt, K., Dikty, S., Ebojie, F., Jones, A., Noël, S., Rozanov, A., and Sinnhuber, B.-M.: Indications for long-term trends and seasonal variations in the SCIAMACHY Level 1 version 6.03 tangent height information, Techn. Note IUP scia pointing 2009-01, Issue 2, University of Bremen, Bremen, Germany, 2009. 10848

Wang, Y. F. and Yuan, Y. X.: A trust region algorithm for solving distributed parameter identification problem, J. Comp. Mathem., 21, 759–772, 2003. 10839, 10840

Witt, G., Stegman, J., Solheim, B. H., and Llewellyn, E. J.: A measurement of the O_2 ($b^1\Sigma_g^+ - X^3\Sigma_g^-$) atmospheric band and the OI(^{1}S) green line in the nightglow, Planet. Space Sci., 27, 341–350, 1979. 10858

Yoshimura, R., Iwagami, N., and Oyama, K.-I.: Rocket measurement of electron density and atomic oxygen density modulated by atmospheric gravity waves, Adv. Space Res., 32, 837–842, doi:10.1016/SO273-1177(03)00422-8, 2003. 10831

AMTD
7, 10829–10881, 2014

Table 1. Photochemical reactions according to the 2-step Barth transfer scheme (see reactions 1, 2 and the resulting reaction 10 for the green line emission) accompanied by quenching. The quantities listed in the column named *intermediate coefficients* correspond to the notation by Khomich et al. (2008) and the coefficients employed here (see Eq. 15) follow the notation by Gobbi et al. (1992) and McDade et al. (1986) and are listed in the column entitled *used coefficients*. See Sect. 5 for further in details.

Item #	Chemical Reaction	Intermediate coefficient	Used coefficient
1	$O(^3P) + O(^3P) + (O_2, N_2) \rightarrow O_2^* + (O_2, N_2)$	α_{O_2}	κ_1
2	$O_2^* + O(^3P) \rightarrow O_2 + O(^1S_0)$	α_O	C(1)
3	$O_2^* + O(^3P) \rightarrow O_2 + O(^3P)$	β_O^*	
4	$O_2^* + N_2 \rightarrow O_2 + N_2$	$\beta_{N_2}^*$	C(2)
5	$O_2^* + O_2 \rightarrow O_2 + O_2$	$\beta_{O_2}^*$	
6	$O_2^* \rightarrow O_2 + h\nu$	A^*	C(0)
7	$O(^1S_0) + O(^3P) \rightarrow 2O(^3P, ^1D_2)$	β_O	${}^1\kappa_5$
8	$O(^1S_0) + N_2 \rightarrow O(^3P, ^1D_2) + N_2^*$	β_{N_2}	${}^2\kappa_5$
9	$O(^1S_0) + O_2 \rightarrow O(^3P, ^1D_2) + O_2^*$	β_{O_2}	${}^3\kappa_5$
10	$O(^1S_0) \rightarrow O(^1D_2) + h\nu(\lambda = 557.7\,\text{nm})$	A_{558}	
11	$O(^1S_0) \rightarrow O(^3P_1) + h\nu(\lambda = 297.2\,\text{nm})$	A_{297}	A_{1S}
12	$O(^1S_0) \rightarrow O(^3P_2) + h\nu(\lambda = 295.8\,\text{nm})$	A_{296}	

AMTD
7, 10829–10881, 2014

Table 2. Einstein coefficients (A_{558}, A_{1S}), excitation parameters (C(0), C(1), C(2)) and factors (k_1, $^1k_5$, $^2k_5$, $^3k_5$) for rate coefficients (κ_1, $^1\kappa_5$, $^2\kappa_5$, $^3\kappa_5$). The values are presented in the Table according to their position in the Eq. (15) that gives the retrieved atomic oxygen concentration (see Table 1, Sect. 5 and Appendix for details).

[O] error bound	A_{558}	A_{1S}	C(0)	C(1)	C(2)	k_1	$^1k_5$	$^2k_5$	$^3k_5$
−1	$1.26\,s^{-1}$	$1.105\,s^{-1}$	9	204	14	5.051	4.467	4.5	1.38
0	$1.16\,s^{-1}$	$1.228\,s^{-1}$	13	224	17	4.700	5.000	5.0	2.32
+1	$1.06\,s^{-1}$	$1.350\,s^{-1}$	17	244	20	4.349	5.533	5.5	3.26

AMTD
7, 10829–10881, 2014

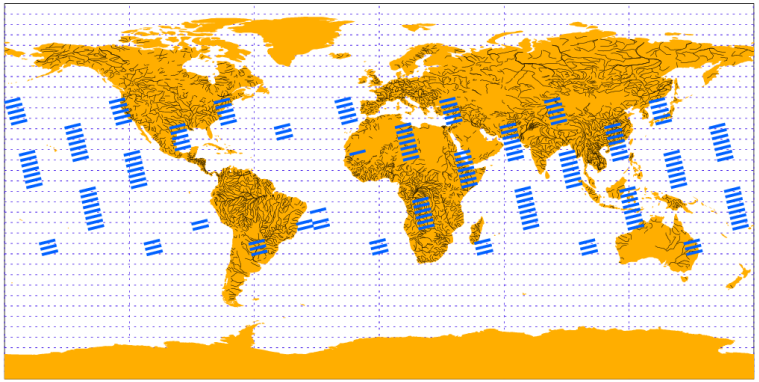

Figure 1. Geographical location and coverage of night-time limb emission observations performed by SCIAMACHY on 9 September 2010 in the dedicated mesosphere/thermosphere mode.

AMTD
7, 10829–10881, 2014

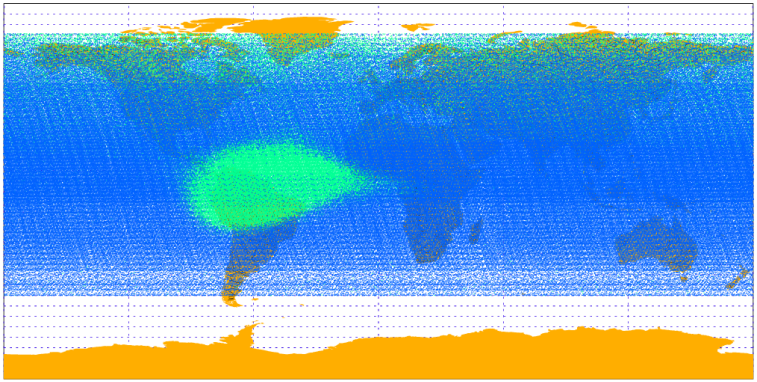

Figure 2. Geographical locations of night-time limb emission observations performed by SCIAMACHY between 2 August 2002 and 8 April 2012. Limb measurements marked in green are excluded because they are affected by Aurora Borealis, highly energetic particles in the South Atlantic Anomaly or by an enhanced offset possibly related contaminating emissions associated with the OH(7-1) transition (Blackwell et al., 1960) and the NO + O air-afterglow continuum (e.g., von Savigny et al., 1999).

AMTD
7, 10829–10881, 2014

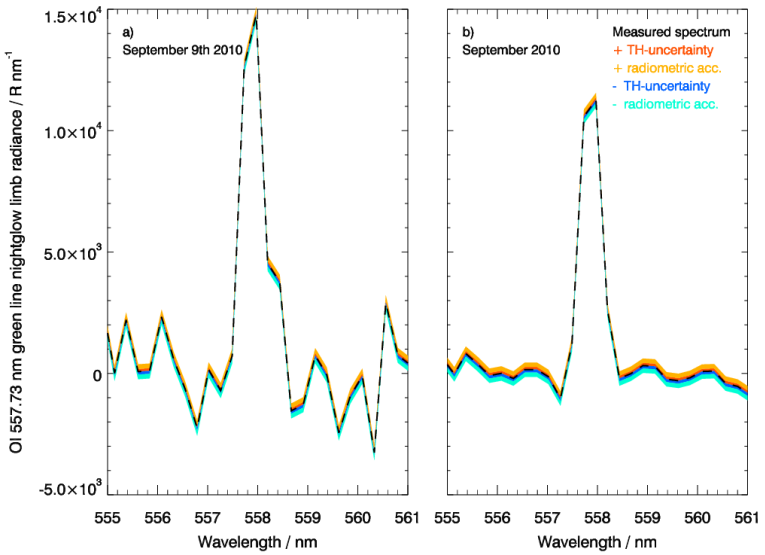

Figure 3. Sample daily **(a)** and monthly **(b)** averaged green line emission spectra at 95 km altitude for the 20–25° N latitude range with uncertainty components σ_h^+ (orange), σ_a^+ (red), σ_h^- (light blue), σ_a^- (blue). See Sects. 3 and 6.1 for further details.

AMTD
7, 10829–10881, 2014

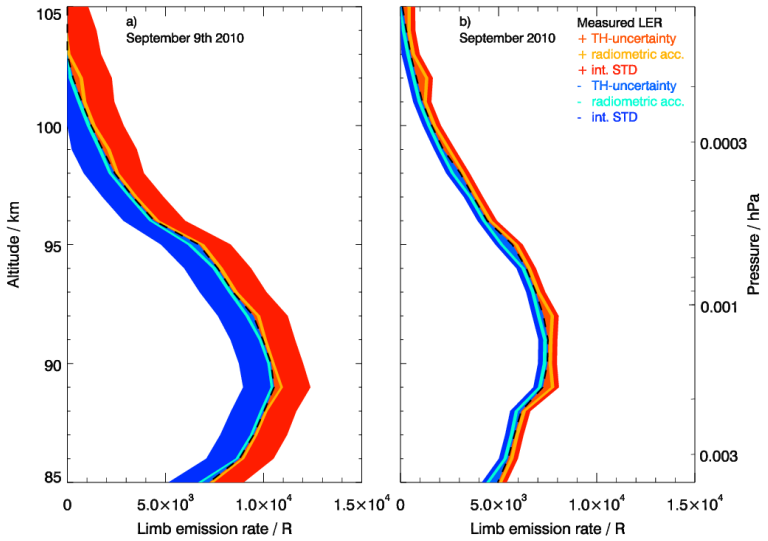

Figure 4. Sample daily **(a)** and monthly **(b)** averaged green line limb emission rate (LER) profiles for the 20–25° N latitude range with uncertainty components σ_h^+ (orange), σ_a^+ (red) introduced for determining P_{+1} and calculated for LER_{+1} and σ_I (yellow) calculated directly for LER_{+1}. Similarly σ_h^- (light blue), σ_a^- (blue) are introduced when calculating P_{-1} and are propagated to determine LER_{-1}. σ_I (cyan) is directly calculated for LER_{-1}. See Sects. 3 and 6.1 for further details.

AMTD
7, 10829–10881, 2014

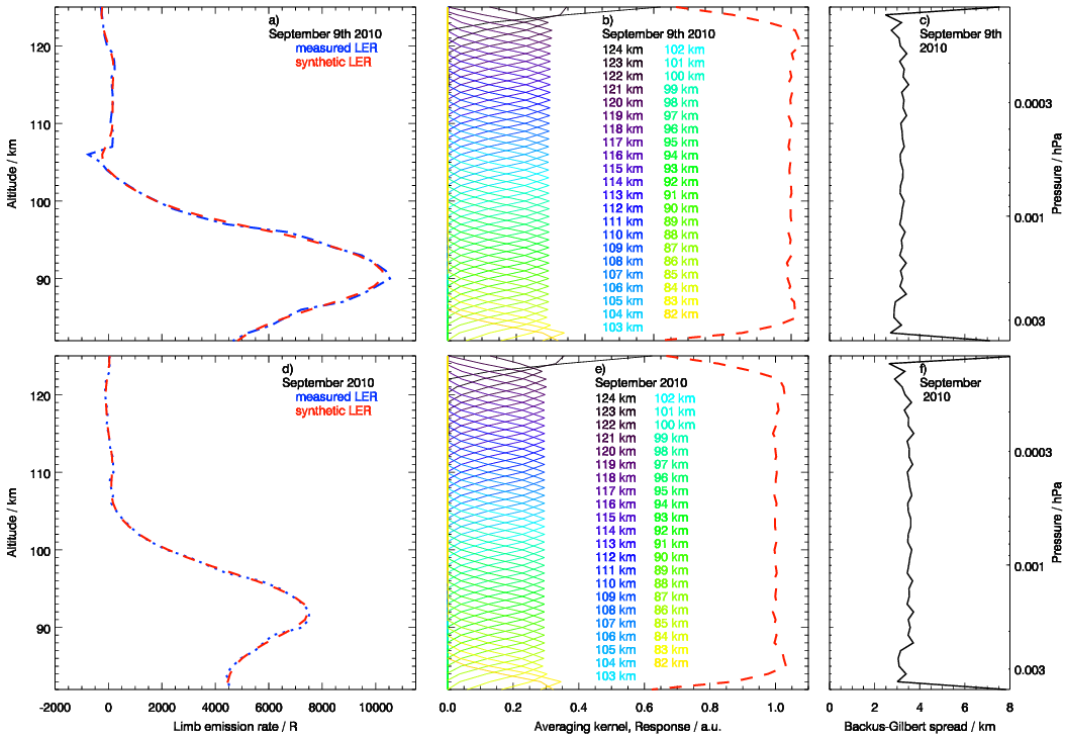

Figure 5. Characteristics and diagnostics of the inversion procedure in sample daily (top row) and monthly averages (bottom row) for the latitude range 20–25° N: comparison of the measured limb emission rate (LER) profile and the synthetic LER profile (panels **a** and **d**); averaging kernel and the resulting area (response curve marked red) (panels **b** and **e**); the vertical resolution (Backus–Gilbert spread) (panels **c** and **f**).

AMTD
7, 10829–10881, 2014

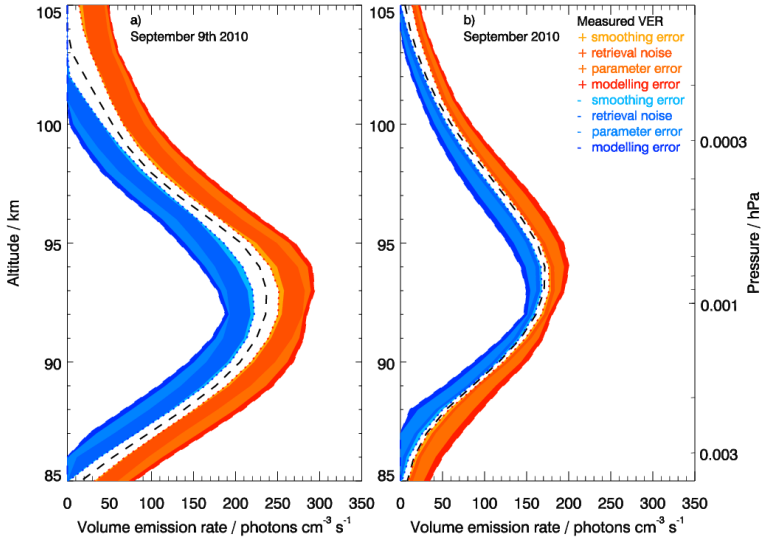

Figure 6. Sample daily **(a)** and monthly **(b)** averaged green line volume emission rate (VER) profiles for the 20–25° N latitude range with uncertainty ($\sigma_{S_{tot}}$) components σ_{S_s} (yellow), σ_{S_m} (orange), σ_{S_b} (light red), σ_{S_f} (red) introduced and calculated for the VER_{+1} retrieval, σ_{S_s} (cyan marked), σ_{S_m} (dark cyan), σ_{S_b} (light blue), σ_{S_f} (blue) introduced and calculated for the VER_{-1} retrieval.

AMTD
7, 10829–10881, 2014

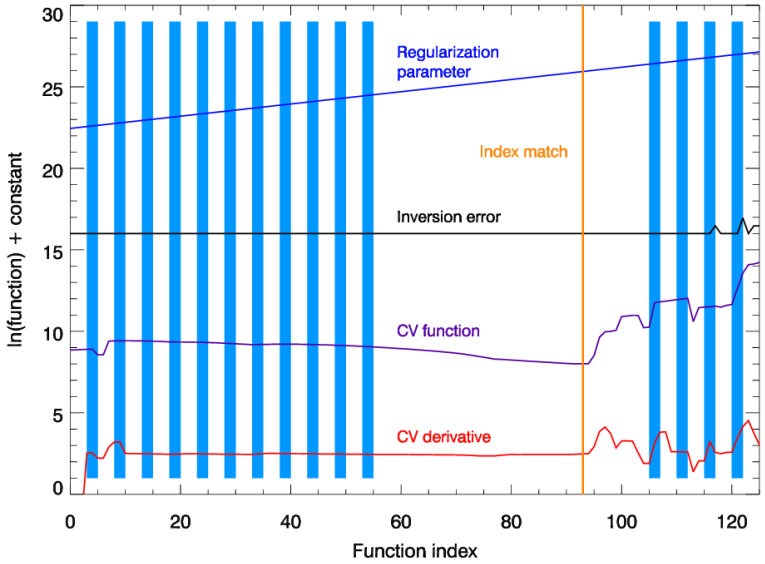

Figure 7. Illustration of the regularized total least squares (RTLS) minimization used for the identification of the optimal regularization parameter γ_r. The cross-validation (CV) function (see Eq. 9) is used to locate its minimum and to determine the index of γ_r. Alternatively, the peak of the CV derivative occurring where the steepest slope of the CV function occurs can be used to locate the index of γ_r. The index of the optimal regularization parameter γ_r is marked by an orange line.

AMTD
7, 10829–10881, 2014

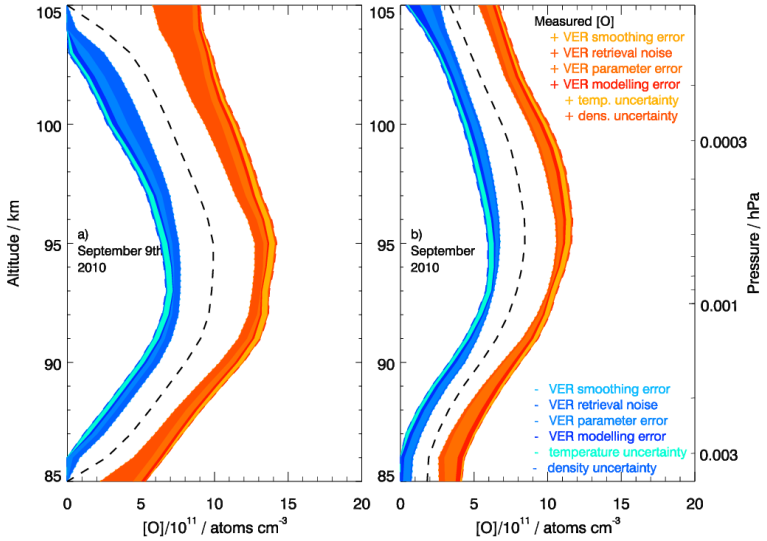

Figure 8. Sample daily **(a)** and monthly **(b)** averaged atomic oxygen concentration ($[O^{quench}_{SABER}]$) profiles for the 20–25° N latitude range with uncertainty components σ_{S_s} (yellow), σ_{S_m} (orange), σ_{S_b} (light red), σ_{S_f} (red) introduced for retrieving VER_{+1} and propagated to $[O]_{+1}$, and σ^{+}_{TD} (yellow) calculated directly for the determination of $[O]_{+1}$. Similarly, σ_{S_s} (cyan), σ_{S_m} (dark cyan), σ_{S_b} (light blue), σ_{S_f} (blue) are introduced for calculating VER_{-1} and are propagated to $[O]_{-1}$, while σ^{-}_{TD} (yellow) is directly calculated when determining $[O]_{-1}$. See Sects. 5, 6.2 and 7.1 for further details.

AMTD
7, 10829–10881, 2014

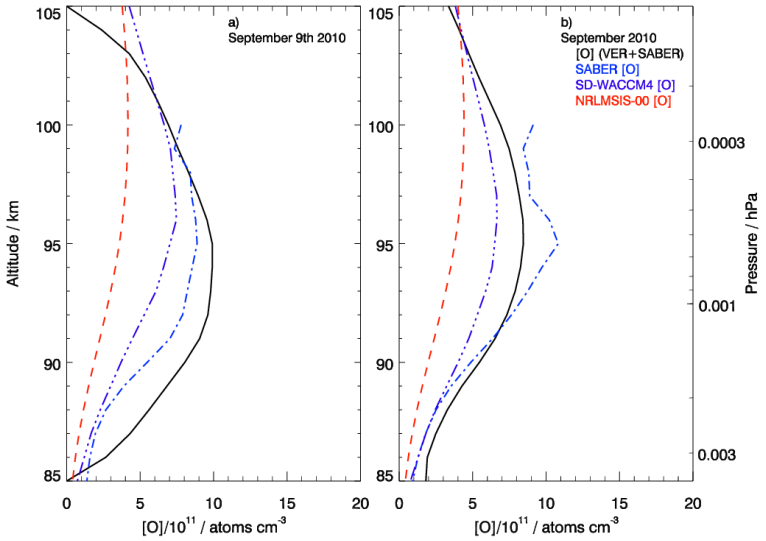

Figure 9. Sample daily **(a)** and monthly **(b)** averaged atomic oxygen concentration profiles (black solid [O^{quench}_{SABER}]) compared with profiles measured by SABER (blue dash dot [O^{SABER}]), and modelled with SD-WACCM4 (violet dash dot dot dot [O^{WACCM4}]) and NRLMSISE-00 (red dashed [O^{MSIS00}]) for the 20–25° N latitude range and at local times between 21:00 and 23:00.

AMTD
7, 10829–10881, 2014

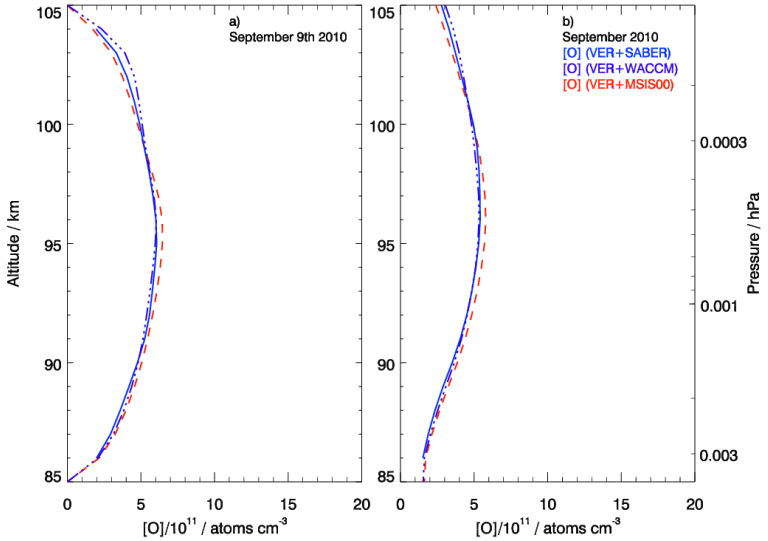

Figure 10. Sample daily **(a)** and monthly **(b)** averaged atomic oxygen concentration profiles ($[O^{cubic}_{SABER}]$ – blue solid, $[O^{cubic}_{WACCM4}]$ – violet dash-dotted, $[O^{cubic}_{MSIS00}]$ – red dashed) according to the cubic equation (McDade et al., 1986), for different sources of background atmospheric profiles and for the 20–25° N latitude range.

AMTD
7, 10829–10881, 2014

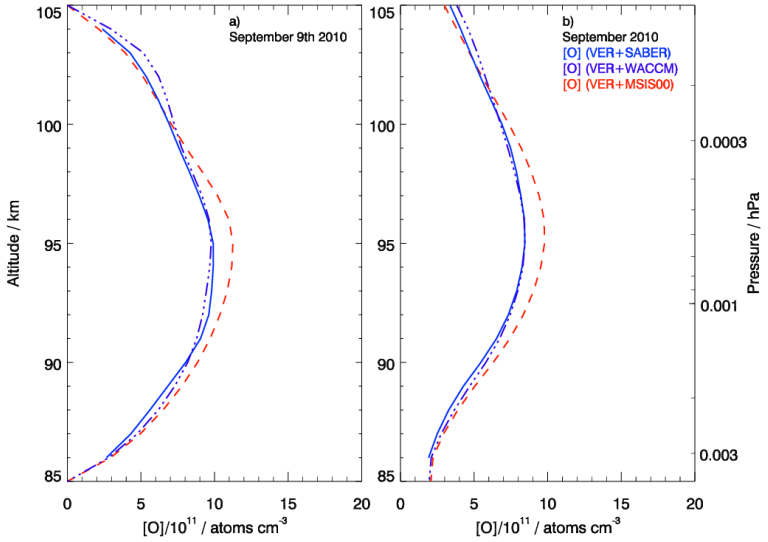

Figure 11. Sample daily **(a)** and monthly **(b)** averaged atomic oxygen concentration profiles ($[O^{quench}_{SABER}]$ – blue solid, $[O^{quench}_{WACCM4}]$ – violet dash-dotted, $[O^{quench}_{MSIS00}]$ – red dashed) according to the extended cubic equation by Gobbi et al. (1992) and Khomich et al. (2008), for different sources of background atmospheric profiles and for the 20–25° N latitude range.

AMTD
7, 10829–10881, 2014

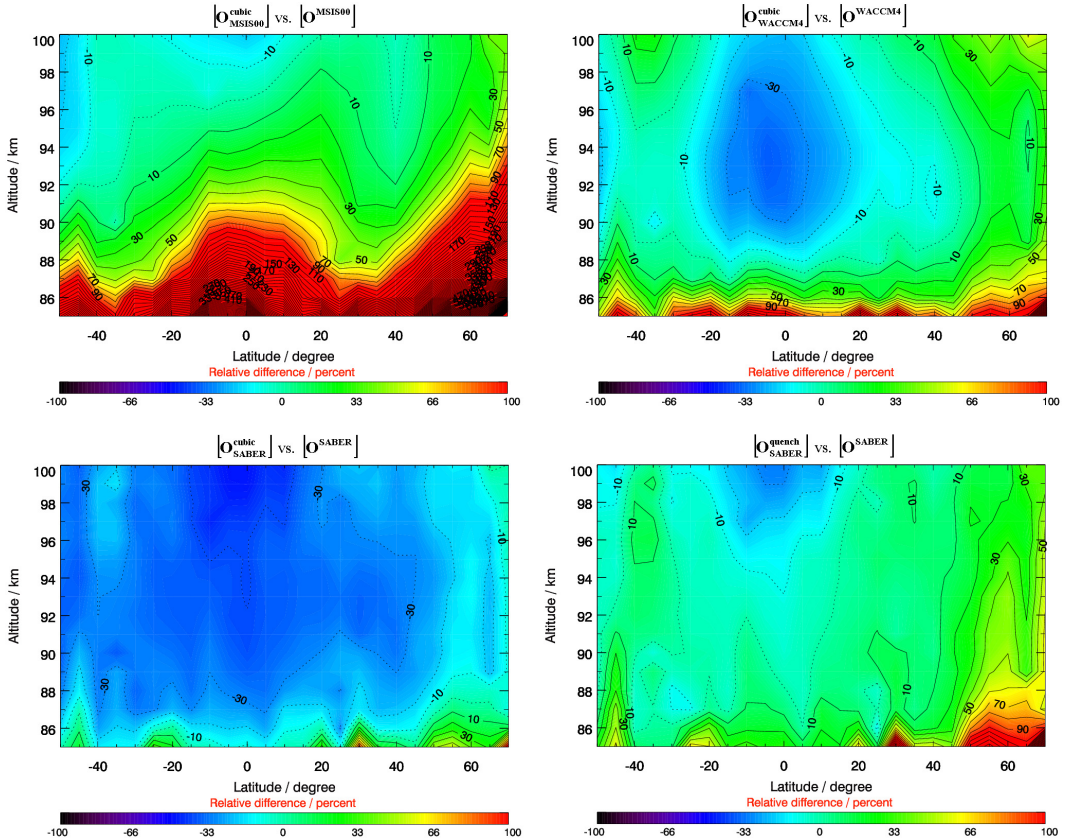

Figure 12. Relative differences in monthly averaged atomic oxygen fields from April 2010 to March 2011: $[O^{cubic}_{MSIS00}]$ compared with reference $[O^{MSIS00}]$ (top left), $[O^{cubic}_{WACCM4}]$ compared with reference $[O^{WACCM4}]$ (top right), $[O^{cubic}_{SABER}]$ compared with reference $[O^{SABER}]$ (bottom left), $[O^{quench}_{SABER}]$ compared with reference $[O^{SABER}]$ (bottom right).

AMTD
7, 10829–10881, 2014

Atomic oxygen retrievals in the MLT region

O. Lednyts'kyy et al.

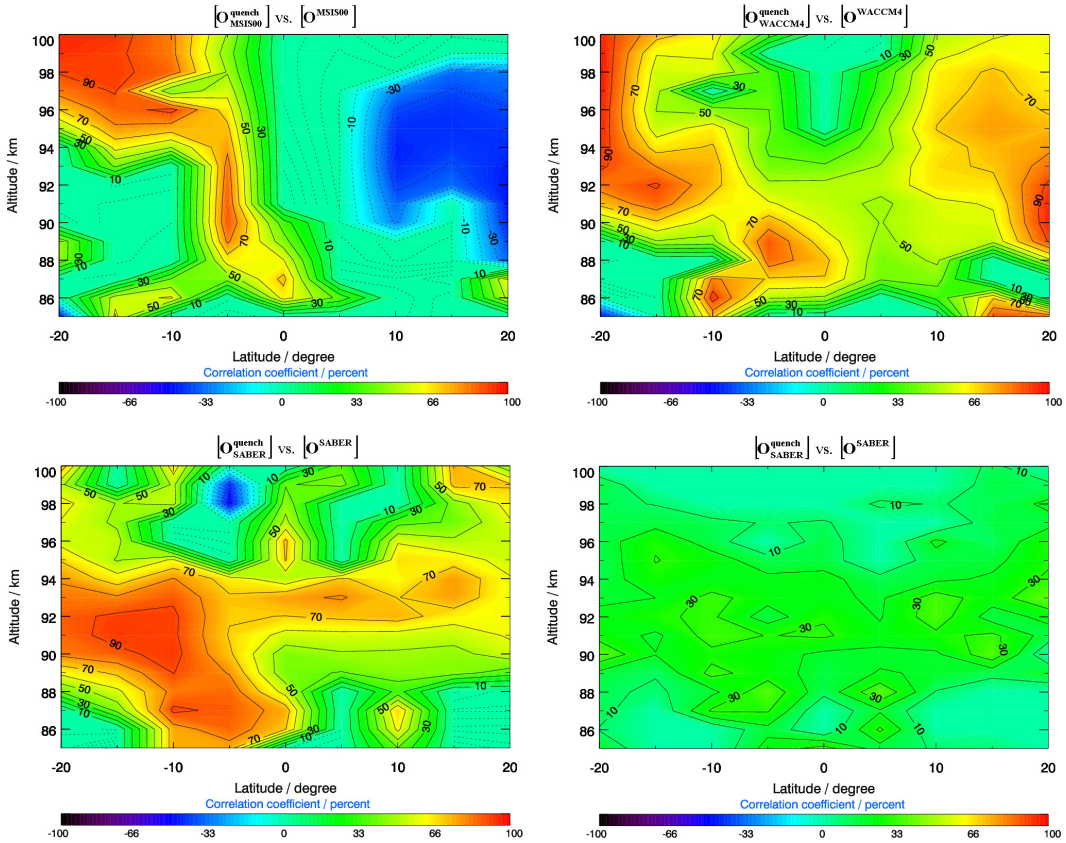

Figure 13. Correlation coefficients for atomic oxygen fields from April 2010 to March 2011: monthly averaged $[O^{quench}_{MSIS00}]$ cross-correlated with $[O^{MSIS00}]$ (top left), monthly averaged $[O^{quench}_{WACCM4}]$ cross-correlated with $[O^{WACCM4}]$ (top right), monthly averaged $[O^{quench}_{SABER}]$ cross-correlated with $[O^{SABER}]$ (bottom left), daily averaged $[O^{quench}_{SABER}]$ cross-correlated with $[O^{SABER}]$ (bottom right).

AMTD
7, 10829–10881, 2014

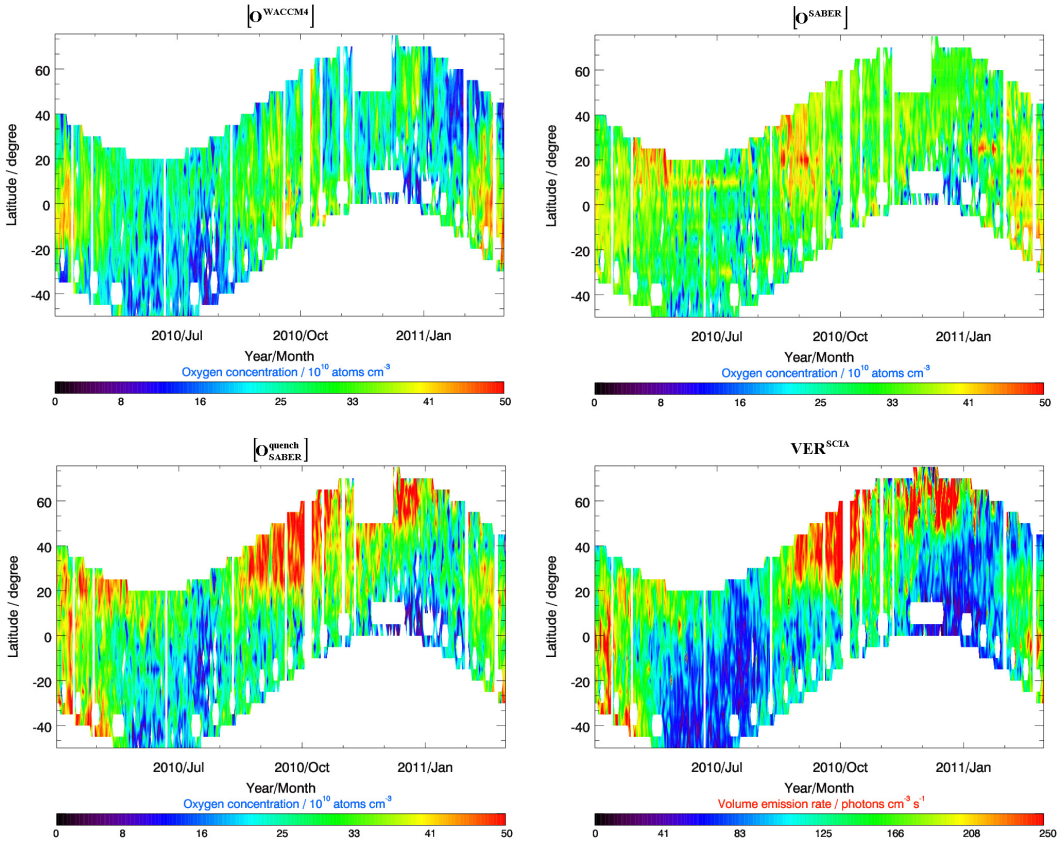

Figure 14. Seasonal variations of daily and vertically averaged (between 85 and 100 km) atomic oxygen fields from April 2010 to March 2011: $[O^{WACCM4}]$ (top left), $[O^{SABER}]$ (top right), $[O^{quench}_{SABER}]$ (bottom left). The bottom right panel shows daily and vertically integrated (also from 85 to 100 km) SCIAMACHY volume emission rates (bottom right).

AMTD
7, 10829–10881, 2014

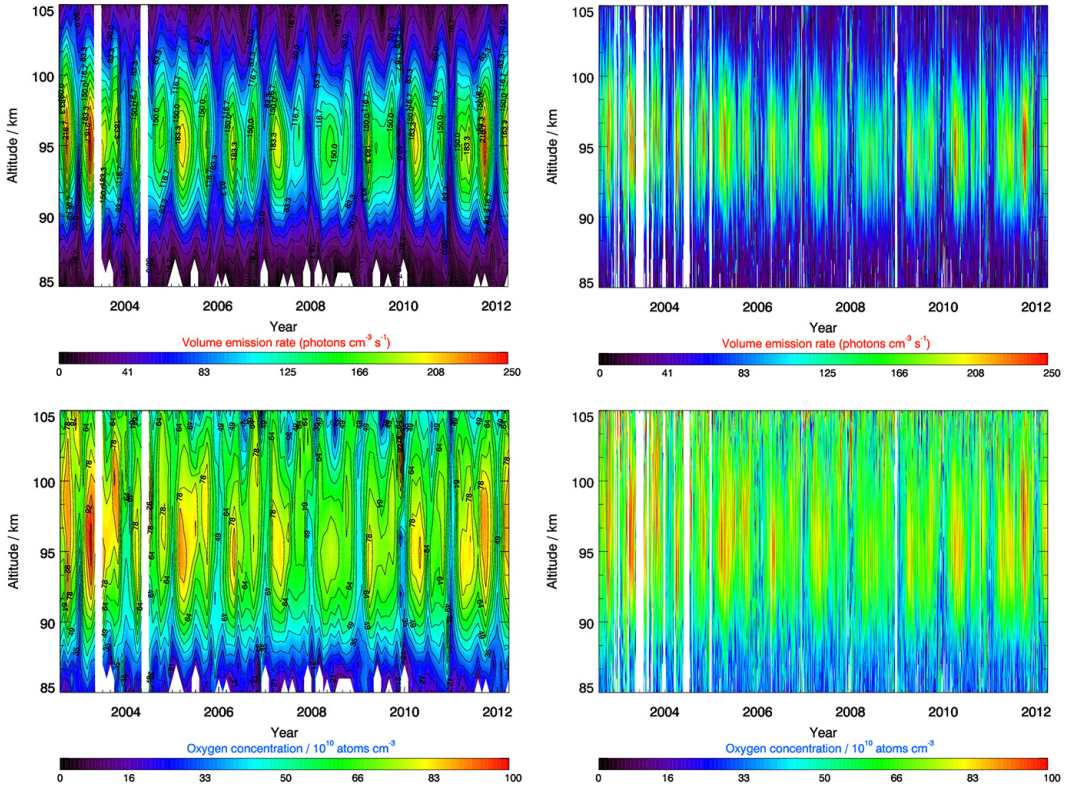

Figure 15. Temporal evolution of VER profiles (top panels) and $[O^{quench}_{SABER}]$ (bottom panels) with monthly (left panels) and daily (right panels) resolution for the 10–20° N latitude range from August 2002 to April 2012.

AMTD
7, 10829–10881, 2014